THE UNIVERSITY
of ADELAIDE

Faculty of Sciences
School of Physical Sciences

Searching for Four Top Quarks with the ATLAS Detector

Emily Filmer

Supervisors:
A/Prof. Paul Jackson
A/Prof. Martin White

February 2020

Declaration

I certify that this work contains no material which has been accepted for the award of any other degree or diploma in my name, in any university or other tertiary institution and, to the best of my knowledge and belief, contains no material previously published or written by another person, except where due reference has been made in the text. In addition, I certify that no part of this work will, in the future, be used in a submission in my name, for any other degree or diploma in any university or other tertiary institution without the prior approval of the University of Adelaide and where applicable, any partner institution responsible for the joint-award of this degree.

I give permission for the digital version of my thesis to be made available on the web, via the University's digital research repository, the Library Search and also through web search engines, unless permission has been granted by the University to restrict access for a period of time.

I acknowledge the support I have received for my research through the provision of an Australian Government Research Training Program Scholarship.

For Dr Colin Frederick Jenner
passionate researcher
scientific pioneer
grandfather
vale

Abstract

The Standard Model predicts the existence of events containing four top quarks, but as yet they have not been experimentally observed. Here, the work focuses on events containing two same-sign leptons, or three leptons. This thesis explores the methods used to look for evidence for the Four Top Standard Model process at the ATLAS detector, at CERN. The optimisation of Boosted Decision Tree algorithms is performed using a multivariate analysis, with the aim of extracting a statistically significant signal strength. To date, the analysis data is still blinded, and as such the final results are not yet available. The four top process is especially interesting because of its relevance to Beyond Standard Model physics relating to the Higgs boson.

In addition, planned upgrades to the ATLAS Inner Tracker subsystem – the Pixel Detector in particular – are discussed with reference to the work being undertaken at the University of Adelaide. These upgrades will allow the University to contribute to the ongoing upgrade work being done on ATLAS by providing an environment where newly built Inner Tracker modules can be tested before they are placed in the detector.

Acknowledgements

My sincere gratitude goes to my supervisors, Paul Jackson and Martin White for their supervision, guidance, and continued passion for Physics. I would also like to thank Frédéric Déliot for his expertise on the Four Top analysis, and who was an invaluable addition to our group in 2019. Thank you to Oğul, for his advice, and help with the BDT code.

Profound love and thanks to my parents for the unwavering support and enthusiasm they have given me over the years.

To my colleagues, especially Red, Abhishek, and Jason, for all their advice, support, jokes, and tea.

To my friends, who have remained appropriately enthusiastic after all this time, despite my best efforts.

Contents

Chapter 1

Introduction

Particle physics is an ever-evolving area of study. The development of high energy accelerator experiments and improvement of computing resources have enabled data collection and processing at a never-before-seen scale. With imminent upgrades to the ATLAS Detector at CERN, additional demands will be required of the hardware and software that will be installed, especially in regards to performance under high radiation within the detector, and the high-speed data processing that is vital to physics analyses.

Chapter 2 introduces the Standard Model of particle physics and the gauge field theories that describe fundamental particles and their interactions through Quantum Electrodynamics, Quantum Chromodynamics, Electroweak Symmetry, and the Higgs Mechanism. This then allows for these particles to be defined in the context of the ATLAS detector at the LHC, at CERN, in Chapter 3. Here, an overview of the sub-detector systems are given with reference to their interactions with Standard Model particles.

The main body of this thesis presents work performed on two separate areas of the ATLAS detector.

Chapter 4 discusses the upgrades being performed on the Inner Tracker of the detector, and the role that the University of Adelaide has in developing a test stand for upgrade work to be carried out. The detector upgrades focus on the Pixel Modules and the hardware that is used to test and refine components and data acquisition software on a small scale. Here the work done by the author is presented in the context of the Inner Tracker group's efforts for the upgrades required for the High-Luminosity LHC. This includes technical set-up, and producing documentation.

Chapter 5 presents some of the studies performed as part of the Standard Model Four Top physics analysis. These studies use Boosted Decision Tree algorithms, a type of machine learning, to understand and model the complex background and signal regions in this analysis. Some preliminary fits with Monte Carlo and Asimov data are discussed, however the analysis is not yet complete, and the data fit in the signal region has not been performed. The author's main contribution to this analysis is that of refining the parameters and variables used to train and test the Boosted Decision trees to enhance the model's performance for use in extracting the

signal strength. The four top analysis is motivated by the top quark's strong coupling to the Higgs boson, which makes it an exciting place to explore potential beyond Standard Model physics, such as two-Higgs-doublet models, of which measurement of the four top cross section is of particular importance.

Chapter 2

The Standard Model

The Standard Model of particle physics (SM) is, at present, the best mathematical formulation that exists to describe elementary particles and their interactions, detailing every observable phenomenon in the Universe, aside from gravity and dark matter. It is a quantum field theory which sees theoretical and experimental observations agree to incredibly high precision. The Model treats both the particles and the forces that govern them as point-like, and they are classified predominantly by their angular momentum quantum number, spin. Fermions, the matter particles, have a half-integer spin, and obey Fermi-Dirac statistics, while the force-mediating bosons have integer spin, and obey Bose-Einstein statistics. Figure 2.1a lists the particles, while Figure 2.1b shows the interactions between them.

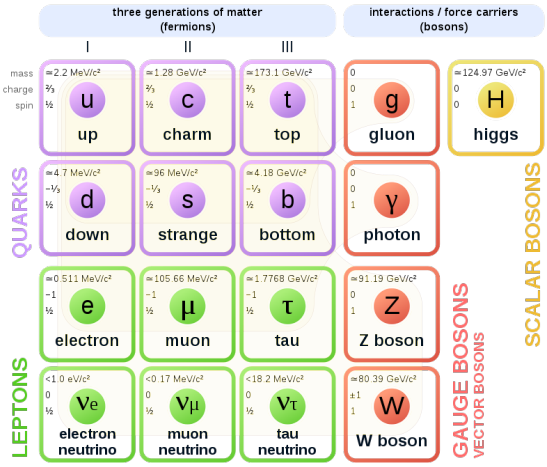

(a) Standard Model Particles [1]

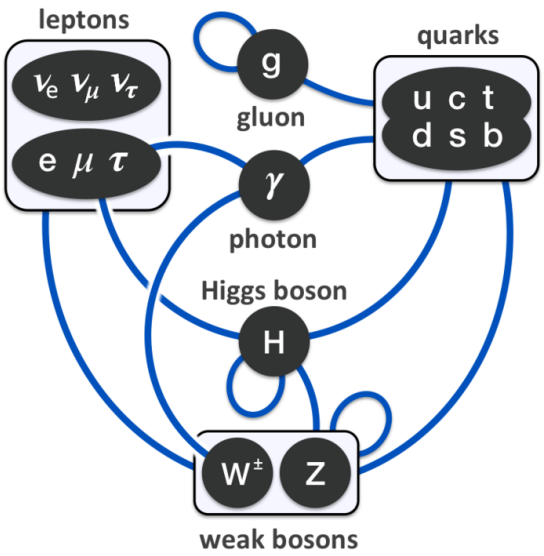

(b) Particle Interactions [2]

Figure 2.1: Constituents of the Standard Model and their interactions. The interactions are shown by the lines between particles.

2.1 Particle Content

2.1.1 Fermions

Fermions are matter particles, and are comprised of six quarks, and six leptons. Mathematically, they are represented by wavefunctions Ψ and $\bar{\Psi}$ for particles and their oppositely-charged antiparticles, respectively. Fermions can also be categorised in three generations, according to mass.

Quarks

Quarks are fermions that experience the strong interaction, as well as electromagnetic and weak interactions. The six quarks each have a unique flavour; up (u), down (d), charm (c), strange (s), top (t), and bottom (b), a property which enables them to experience the weak interaction through the electroweak gauge bosons. The up, charm, and top quarks have an electric charge of $+\frac{2}{3}$ while the down, strange, and bottom have a charge of $-\frac{1}{3}$, and this gives them the ability to interact electromagnetically. Quarks transform as Lie Group $SU(3)$ triplets with the quantum number "colour", experiencing the strong force through the gluons. Due to confinement, quarks can only be observed in bound, colourless states; most commonly either as baryons (qqq) or mesons ($q\bar{q}$), known as hadrons. Only u and d quarks are light enough to form stable hadronic matter that can be directly detected, and while the s, c, and b quarks can form hadrons, they only live briefly before decaying into lighter fermions. The heaviest quark is the top, and it is so short-lived that it decays before it can hadronise, as will be further discussed in Chapter 5.

Leptons

Leptons, too, have six flavours; electron (e) and electron neutrino (ν_e), muon (μ) and muon neutrino (ν_μ), and tau (τ) and tau neutrino (ν_τ). Leptons do not carry colour charge, but do interact via the weak force with other fermions. In addition, e, μ, and τ carry electric charge and can interact electromagnetically. Muons and taus are unstable and decay into lighter leptons, whereas electrons, the lightest charged lepton, are stable and directly observable. Neutrinos interact so weakly with other Standard Model particles that they are difficult to directly detect in most experiments, and in collider experiments their presence is inferred from missing energy and lepton number conservation. Missing energy will be explicitly defined in Section 3.2.

2.1.2 Gauge Bosons

Gauge bosons are the force mediators of the Standard Model. The eight gluons (g) mediate the strong force 2.2.2, the photon (γ) mediates the electromagnetic force 2.2.1, and three weak gauge bosons (W^+, W^-, and Z) mediate the weak interaction.

The Higgs boson is discussed separately in 2.2.4. Photons and gluons are massless, whereas the electroweak bosons are massive.

W Bosons

The charged $W^{\pm}$ bosons have a mass of 80.4 Gev [3] [4] . This charge allows them to give rise to flavour-changing current. The Cabibbo-Kobayashi-Maskawa (CKM) Matrix describes the flavour-changing weak interaction strength of (u, c, t) coupling to (d, s, b) quarks. The best current approximation of these values [4] are

$$\begin{bmatrix} |V_{ud}| & |V_{us}| & |V_{ub}| \\ |V_{cd}| & |V_{cs}| & |V_{cb}| \\ |V_{td}| & |V_{ts}| & |V_{tb}| \end{bmatrix} \approx \begin{bmatrix} 0.974 & 0.225 & 0.004 \\ 0.224 & 0.974 & 0.042 \\ 0.009 & 0.041 & 0.999 \end{bmatrix} \tag{2.1}$$

Here, it is most important to note that the diagonal terms are close to unity, which shows that when undergoing weak transitions, quarks will prefer, where possible, to remain in the same generation. This is especially important when considering the decay of top quarks in Chapter 5.

Z Bosons

Z bosons have a mass of 91.19 GeV [4], and are uncharged. This means that they can mediate weak decay, but cannot change the flavours of leptons involved, as the Standard Model does not contain flavour-changing neutral currents.

2.2 Gauge Field Formulation of the Standard Model

The Standard Model is a Gauge Field Theory with external and internal symmetries. The external symmetries are space-time symmetries and fall under the Poincaré group and the internal symmetries are Gauge Symmetries. The SM uses symmetries described by the continuous Lie Groups; $SU(3)_C \otimes SU(2)_L \otimes U(1)_Y$, where $SU(3)_C$ describes the strong force (colour), and $SU(2)_L \otimes U(1)_Y$ the electroweak force. This section gives an overview of the mathematical formulation of the Standard Model through gauge invariant symmetries by considering Quantum Electrodynamics, Quantum Chromodynamics, Electroweak Symmetry, and the Higgs Mechanism of Electroweak Symmetry Breaking.

The Standard Model Lagrangian is given by

$$\mathcal{L}_{SM} = -\frac{1}{4}F_{\mu\nu}F^{\mu\nu} + i\bar{\Psi}\not{D}\Psi + \psi_i y_{ij}\psi_j\phi + |D_\mu\phi|^2 - V(\phi) \tag{2.2}$$

where

- $-\frac{1}{4}F_{\mu\nu}F^{\mu\nu}$ describes the self-interactions between the $W^{\pm}$ and Z^0 bosons, and gluon self-interaction,

- $i\bar{\Psi}\not{D}\Psi$ describes how fermions interact with gauge bosons,
- $\psi_i y_{ij} \psi_j \phi$ gives rise to fermion masses through the interaction between fermions and the Higgs boson,
- $|D_\mu \phi|^2$ gives rise the gauge bosons' mass through interaction with the Higgs field,
- $V(\phi)$ describes the spontaneous symmetry breaking of the electroweak sector into its electromagnetic and weak sections, generates the Higgs mass, and governs Higgs self-interaction.

2.2.1 Quantum Electrodynamics

Quantum Electrodynamics, QED, is a gauge field theory that describes the properties of electrically charged particles and the photon. It is globally gauge invariant, and the free fermionic field is described by the Dirac Lagrangian;

$$\mathcal{L} = i\bar{\Psi}\gamma^\mu \partial_\mu \Psi - m\bar{\Psi}\Psi \tag{2.3}$$

For local gauges,

$$\Psi \rightarrow e^{i\theta(x)}\Psi \tag{2.4}$$

This produces an extra term in the Lagrangian, but invariance can be restored through the introduction of a field, A_μ, so that

$$\begin{aligned} \mathcal{L} &\rightarrow \mathcal{L} - g_e \bar{\Psi}\gamma^\mu A_\mu \Psi & (2.5)\\ \text{and} \quad A_\mu(x) &\rightarrow A_\mu(x) - \partial_\mu \alpha(x) & (2.6)\\ \text{where} \quad \alpha(x) &= -\frac{\theta(x)}{g_e} \end{aligned}$$

A free term is then required to make A_μ both gauge invariant and propagating, using $F_{\mu\nu} = (\partial_\mu A_\nu - \partial_\nu A_\mu)$ as the electromagnetic field tensor,

$$\mathcal{L} = -\frac{1}{4} F_{\mu\nu} F^{\mu\nu} \tag{2.7}$$

Any mass terms for the gauge boson are forbidden, since they would violate gauge invariance. This condition imposes the massless property of the photon field, which has been experimentally verified to be $m_\gamma < 1 \times 10^{-18}$ eV [4].

The whole QED Lagrangian can then be written

$$\mathcal{L}_{\text{QED}} = \bar{\Psi}(i\gamma^\mu \mathcal{D}_\mu - m)\Psi - \frac{1}{4} F_{\mu\nu} F^{\mu\nu} \tag{2.8}$$

where $\mathcal{D}_\mu$ is the covariant derivative, $\mathcal{D}_\mu = \partial_\mu + i g_e A_\mu$.

In practice, this shows that the photon, γ, the force carrier for Quantum Electrodynamics, is uncharged, and that its coupling energy is proportional to the scale of its interaction.

2.2.2 Quantum Chromodynamics

The existence of baryons, qqq, and mesons, $q\bar{q}$, require a different gauge field theory to satisfy Fermi-Dirac statistics, which in turn requires a new quantum number. Quantum Chromodynamics (QCD) uses colour to describe the interactions between the six quarks and eight gluons, which arise from imposing a gauge invariance related to the $SU(3)$ group. In addition, quarks take on one of three colours, (red, green, blue), and quarks must conform to colour confinement, as either mesons or baryons, which are colourless bound states. Much like in QED, the QCD Lagrangian can be seen in the form

$$\mathcal{L}_{QCD} = \bar{\Psi}(i\gamma^{\mu}\mathcal{D}_{\mu} - m)\Psi - \frac{1}{4}F^{a}_{\mu\nu}F^{\mu\nu}_{a} \tag{2.9}$$

with covariant derivative

$$\mathcal{D}_{\mu} = \partial_{\mu} + ig_{s}\frac{\lambda^{a}}{2}A^{a}_{\mu} \tag{2.10}$$

where $a = 1, ..., 8$ for the eight gluon fields A^{a}_{μ}, g_s is the coupling constant for the strong force, and λ^{a} are the Gell-Mann matrices.

2.2.3 Electroweak Symmetry

The electromagnetic and weak forces are unified under $SU(2)_L \times U(1)_Y$ to arrive at an electroweak force. The $SU(2)_L$ acts on isospin (quantum number for weak interactions) for left-handed leptons which are represented as the doublets

$$\psi_L = \begin{pmatrix} \nu_e \\ e \end{pmatrix}_L, \begin{pmatrix} \nu_\mu \\ \mu \end{pmatrix}_L, \begin{pmatrix} \nu_\tau \\ \tau \end{pmatrix}_L \tag{2.11}$$

$U(1)_Y$ transformations act on hypercharge Y,

$$Y = Q - \frac{I_3}{2} \tag{2.12}$$

where Q is the electric charge and I_3 is the 3rd component of weak isospin. For three gauge bosons W_μ associated with $SU(2)_L$, and one gauge boson B^μ associated with $U(1)_Y$, the Lagrangian takes the form

$$\mathcal{L}_{EW} = \bar{\Psi}(i\gamma^{\mu}\mathcal{D}_{\mu} - m)\Psi - \frac{1}{4}W_{\mu}W^{\mu} - \frac{1}{4}B_{\mu}B^{\mu} \tag{2.13}$$

and has a covariant derivative

$$\mathcal{D}_{\mu} = \partial_{\mu} - ig_{Y}YB_{\mu} - ig_{w}\frac{\boldsymbol{\tau}}{2}\boldsymbol{W}_{\mu} \tag{2.14}$$

for weak and electromagnetic coupling constants g_w and g_Y, and $\boldsymbol{\tau}$ the Pauli generators. W_μ is zero for right-handed fields. Despite the gauge bosons having mass, a mass term in the Lagrangian would thus far violate gauge invariance, and so a new mechanism that breaks this electroweak symmetry in the form of a potential field was incorporated. This field is called the Higgs.

2.2.4 Higgs Mechanism

Theorised in 1964 [5] [6] [7], the Higgs boson was experimentally verified in 2012 [8] [9], gaining Peter Higgs and François Englert a Nobel Prize the following year. The requirement of a scalar boson with the properties of the Higgs came about to explain why all other particles (except the photon and gluon) are massive, and to account for the spontaneous symmetry breaking of the electroweak sector. To break this symmetry, a scalar field with a non-zero vacuum expectation value (VEV) is required. Adding four scalar fields ϕ_i as a doublet under weak isospin to the Electroweak Lagrangian in Equation 2.13 produces

$$\mathcal{L} = -\frac{1}{4}(F_{\mu\nu})^2 + (\mathcal{D}_\mu\phi)^\dagger(\mathcal{D}^\mu\phi) - V(\phi^\dagger\phi) \tag{2.15}$$

$$V(\phi) = \mu^2\phi^\dagger\phi + \lambda(\phi^\dagger\phi)^2 \tag{2.16}$$

$$\phi = \frac{1}{\sqrt{2}}\begin{pmatrix}\phi_1 + i\phi_2 \\ \phi_3 + i\phi_4\end{pmatrix} \tag{2.17}$$

For $\mu^2 < 0$, and $\lambda > 0$, this takes the shape of a "Mexican hat" potential in Figure 2.2.

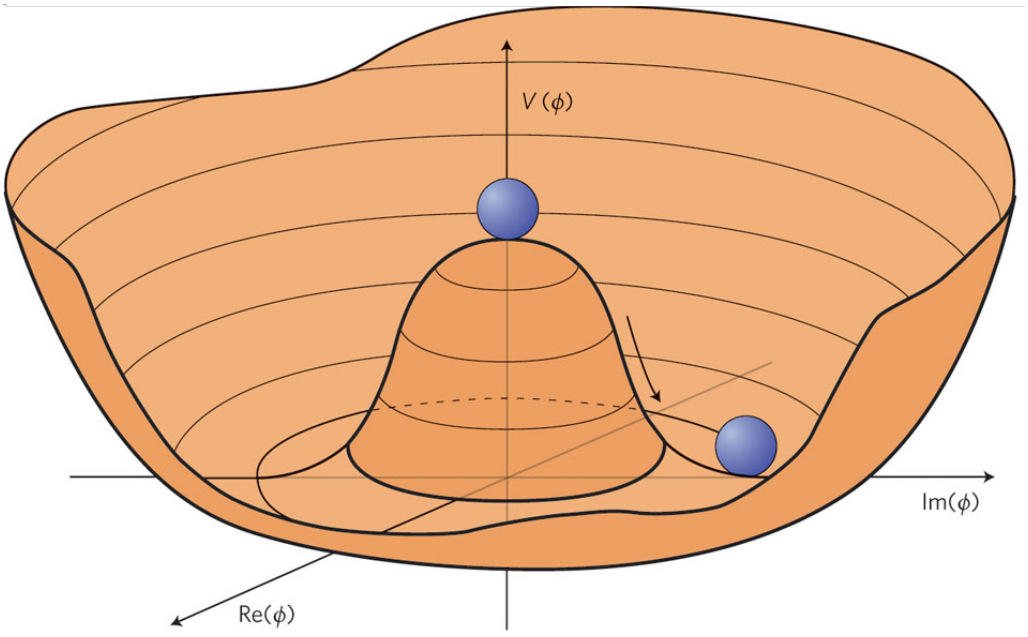

Figure 2.2: The "Mexican hat" potential of the Higgs field [10].

Minimising the infinite number of potential ground states

$$\phi^\dagger\phi = -\frac{\mu^2}{2\lambda} \tag{2.18}$$

and choosing one ground state spontaneously breaks the symmetry, for which the VEV is conventionally written

$$\phi_0 = \frac{1}{\sqrt{2}}\begin{pmatrix}0\\v\end{pmatrix} \tag{2.19}$$

In general form, this becomes

$$\phi = \frac{1}{\sqrt{2}}\begin{pmatrix}0\\v+H(x)\end{pmatrix} \tag{2.20}$$

where $H(x)$ is the Higgs boson, allowed by the gauge invariance of $SU(2)_L$. The Electroweak covariant derivative in Equation 2.14 couples the Higgs field to the $W^\pm$ and Z^0 gauge bosons, giving them mass, as well as to the Higgs boson itself.

The Standard Model is an excellent theoretical description of the fundamental particles and their interactions, however its precision is only known due to experimental verification. Particle physics experiments allow the study of these particles and their properties, and one such experiment, ATLAS, will be discussed in Chapter 3.

Chapter 3

The ATLAS Detector

Particle accelerators enable scientists to experimentally measure Standard Model particles and their properties. The largest such collider is the Large Hadron Collider (LHC), at the European Organisation for Nuclear Research (CERN), which is located underground France and Switzerland. The ATLAS (A Toroidal LHC ApparatuS) detector is the largest detector on the LHC ring. This chapter gives a brief overview of the LHC, ATLAS detector subsystems, the objects defined by ATLAS, and the way that ATLAS physics can be simulated with Monte Carlo events.

3.1 The Large Hadron Collider

A schematic of the LHC, including its pre-accelerators, is shown in Figure 3.1.

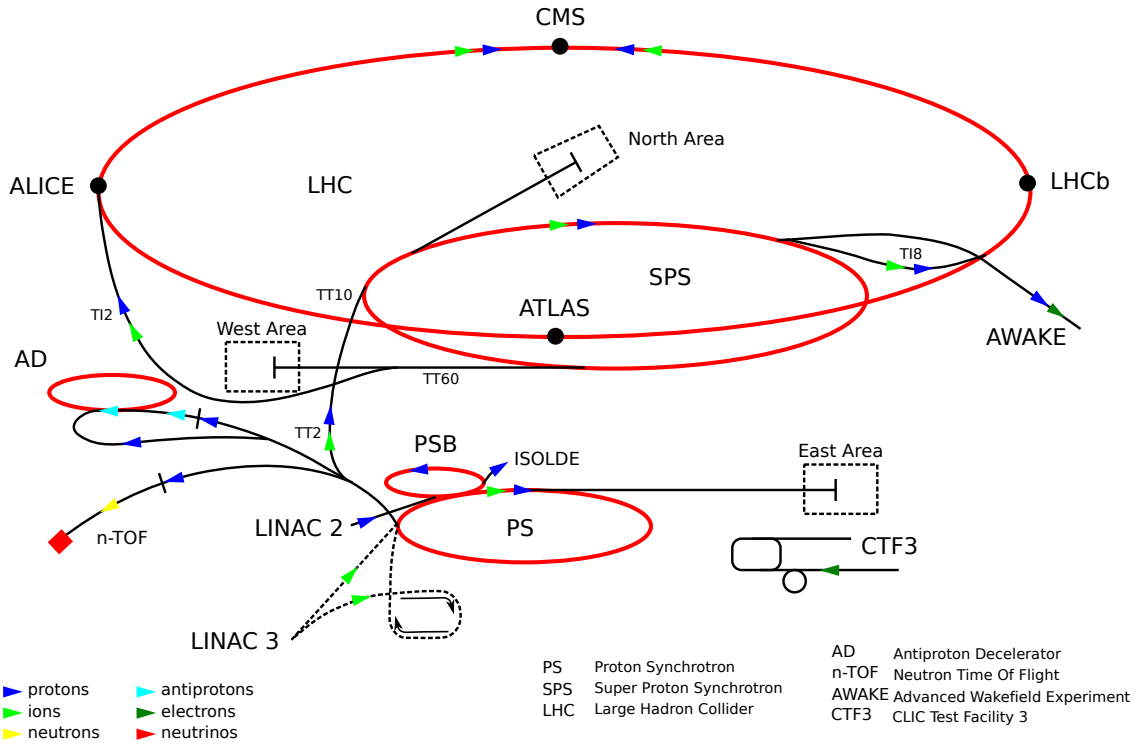

Figure 3.1: The Large Hadron Collider complex at CERN. [11]

Hydrogen atoms are delivered from one end of a linear accelerator, Linac 2, and pass through an electric field where they are ionised and accelerated to 50 MeV [12]. The protons are then accelerated in stages using a system of superconducting magnets in the Proton Synchotron Booster (PSB), Proton Synchotron (PS), and then the Super Proton Synchotron (SPS), which takes the proton energy from 50 Mev to 1.4 Gev to 25 GeV to 450 GeV respectively [13] [14]. The SPS then splits the proton beam into two opposing directions, and injects these beams into the main 27km ring of superconducting magnets, the Large Hadron Collider, where they reach 7 TeV, and 99.99% the speed of light. The beams meet, colliding the protons, at the four main experiments around the ring; ATLAS, CMS, ALICE, and LHCb. Presently, the proton collisions have a centre of mass energy of $\sqrt{s} = 13$ TeV. The data collected is measured as an integrated luminosity, which to date is 139 fb^{-1} for Run II, where data was collected between 2015 and 2018. The remainder of this chapter focuses on the physics of the LHC in the context of the ATLAS detector.

3.1.1 Luminosity

Luminosity is the measurement of the number of particle collisions per unit area for a detector, in this case, the ATLAS detector. One of the main considerations is the cross-sectional area of the particles in the collision, and for the ATLAS detector it is protons. The protons are not isolated, and are transferred around the ring in groups, called bunches.

The instantaneous luminosity, L, is measured by

$$L = \frac{n_{bb} f_b N^2 \gamma}{4\pi\sigma_x\sigma_y} F \tag{3.1}$$

where n_{bb} is the number of bunches, f_b is the bunch crossing frequency, N^2 is the number of protons per bunch, σ_x, σ_y is the transverse size of the beam, γ is to account for the relativistic behaviour of the protons, and F is a geometric factor that reflects the size of the bunch crossing angle. For Run-II of the LHC, $N^2 = (1.15 \times 10^{11})^2$, $\sigma_x\sigma_y = (16 \times 10^{-4})^2$ cm^2, and $f_b = 40 \times 10^6$ s^{-1}. The instantaneous luminosity increased from $L = 5 \times 10^{33}$ cm^{-2} s^{-1} in 2015 to $L = 19 \times 10^{33}$ cm^{-2} s^{-1} in 2018 [15]. Figure 3.2 shows the integrated luminosity over time for Run II of the ATLAS detector.

Luminosity is integrated to give a measure of the number of collisions — and thus data collected — over time, written:

$$\mathcal{L} = \int L dt \tag{3.2}$$

It is measured in units of inverse cross section, the inverse femtobarn, (10^{39} cm^{-2}). From this equation, the number of expected events of a particular process can be found from $N = \sigma L$ where σ is the cross section of the events of interest. Figure 3.4 shows the summary of some Standard Model processes compared to their theoretical

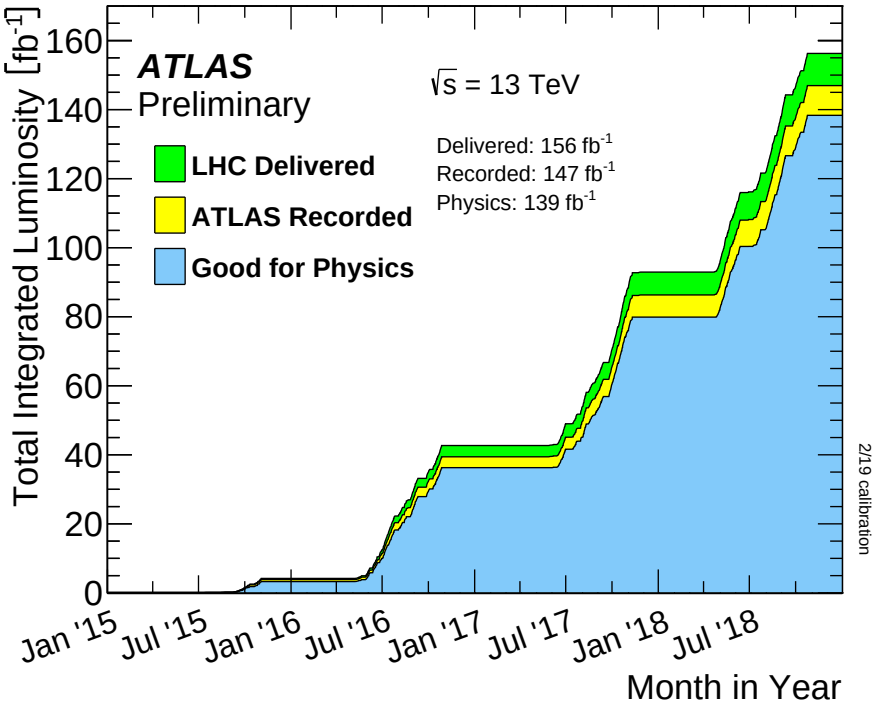

Figure 3.2: Integrated luminosity for Run-II of the ATLAS detector. [16]

expectations from the ATLAS detector. The integrated luminosity for Run-II was $\mathcal{L} = 139$ fb^{-1} [15] and from Figure 3.2 it can be seen that nearly 95% of the luminosity delivered to the ATLAS detector by the LHC was able to be recorded, with the 5% deficit due mostly to pile-up effects.

3.1.2 Pile-Up

While an *event* is the data that is obtained from a particular bunch-crossing, *pile-up* refers to the proton-proton collisions that are present in addition to events. With 30 bunch crossings every 25 ns, pile-up is a important factor to address in both detector design and physics analysis, and will be discussed in later sections.
Vertices are clusters of charged particles, which are grouped by their closest distance to the collision point. These groups can then be used to remove any charged particles that may belong to pile-up, typically those with low momenta. A *primary vertex* is the location of an inelastic p-p collision, of which there may be multiple for each event. A *track* is the path a particle takes from the vertex through the detector [17].

3.2 The ATLAS Detector

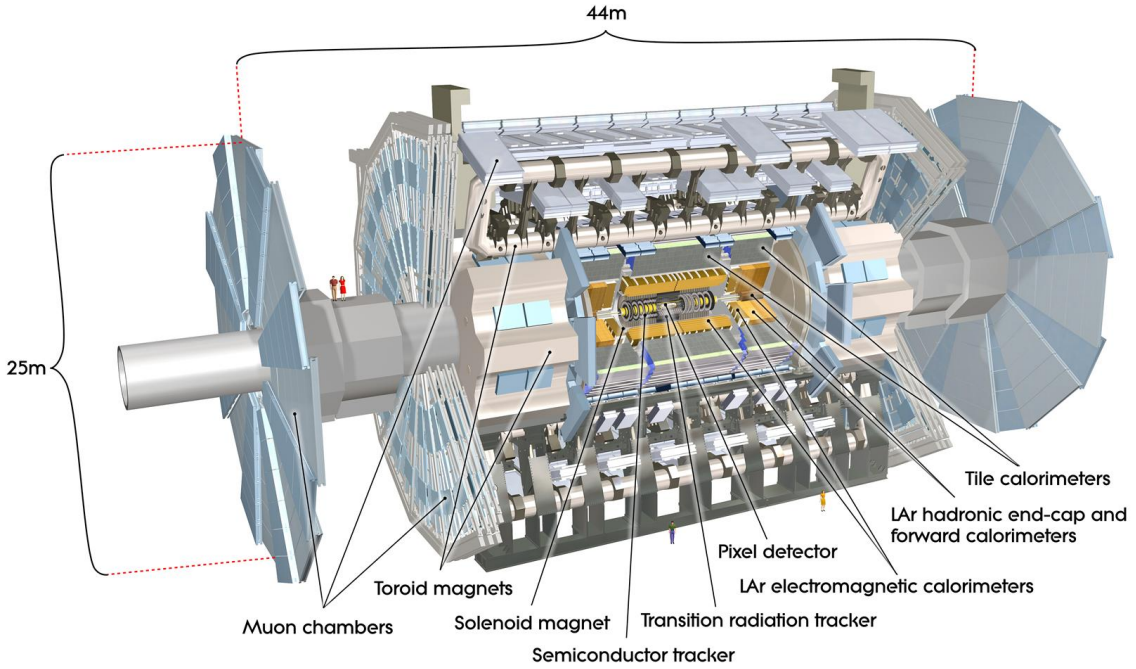

Figure 3.3: The ATLAS detector and its main components. [18]

The ATLAS (A Toroidal LHC ApparatuS) detector [18], Figure 3.3, is the largest of the four detectors on the LHC, and is situated on one of the LHC beam interaction points. It is a general purpose detector with forward-backward symmetry, and is comprised of concentric cylindrical layers, detailed in Figure 3.5. These layers are each responsible for detecting a different particle or property, and the overall four-momentum of decay products is then used to reconstruct physics events. Some of the processes measured by ATLAS are shown in Figure 3.4 with their experimental cross sections (points) overlaid on their theory predictions (bars) where the different colours represent different LHC operation energies.

The detector's coordinates are defined in x, y, z, with a right-hand convention, and the origin being the collision interaction point. The z axis points along the beamline in an anti-clockwise direction. The $x - y$ plane is called the transverse plane, and momentum measured in the plane is referred to as transverse momentum, p_T. Due to the hadronic nature of protons, the centre of mass frame must undergo a Lorentz boost to better confine the collision in $x-y$ space. The cylindrical symmetry of the detector is utilised to measure an azimuthal angle, ϕ, measured around the beam axis, and θ is defined as the polar angle from the beam axis. Conventionally,

pseudorapidity, η, is measured, instead of θ, where

$$\eta = -\ln\tan(\frac{\theta}{2})$$

and distance from the beam interaction point is taken to be $\Delta R = \sqrt{\Delta\eta^2 + \Delta\phi^2}$. Only the four-momentum of muons, electrons, and photons are measurable by the ATLAS detector.

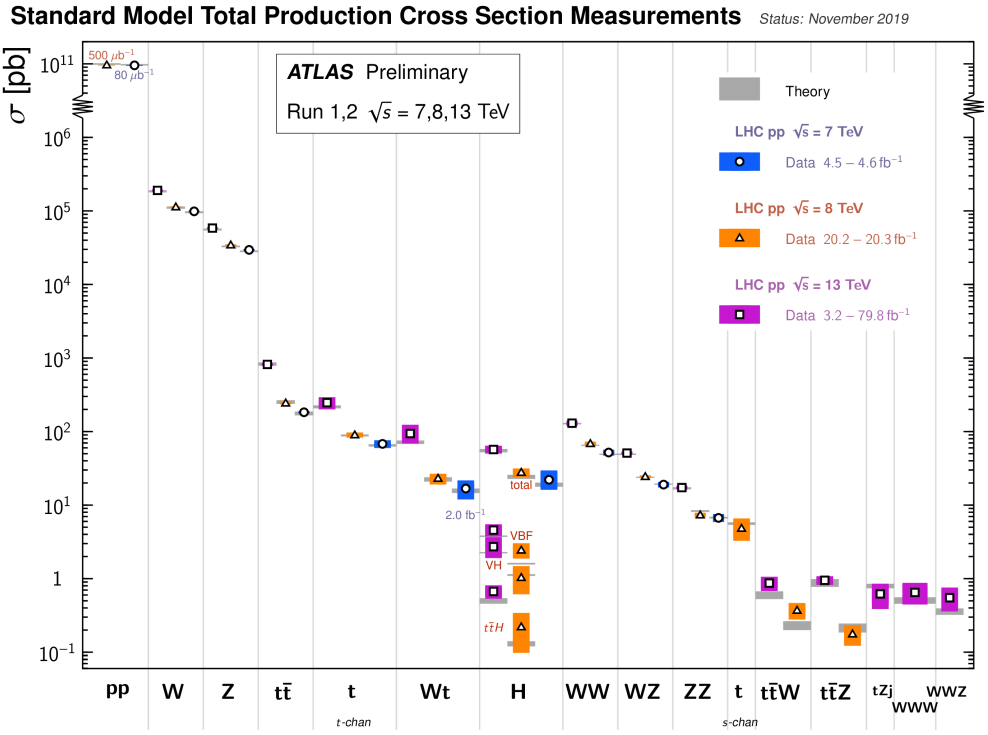

Figure 3.4: Summary of cross section (σ) measurements taken by ATLAS for some Standard Model processes, with their theoretical expectations. [19]

Missing Transverse Momentum

Before collisions take place, there is no momentum in the transverse plane, as protons travel only along the beamline, so the sum over all objects $\sum \vec{p}_T = 0$ for each event. When the four-momentum of physics objects (defined in 3.3) in each event are summed, the result is usually non-zero, and this remaining quantity is denoted $\vec{p}_T^{\,\text{miss}}$ with a modulus that is referred to as the *missing transverse energy*, $E_{\text{T}}^{\text{miss}}$ [21]. In the LHC, and thus in ATLAS, $E_{\text{T}}^{\text{miss}}$ comes from sources including neutrinos (whose interaction with matter is too small to be picked up by the detector), objects whose momentum is lost because they fall outside the detector acceptance, and objects that are poorly reconstructed, leading to an anomalous contribution to the $E_{\text{T}}^{\text{miss}}$.

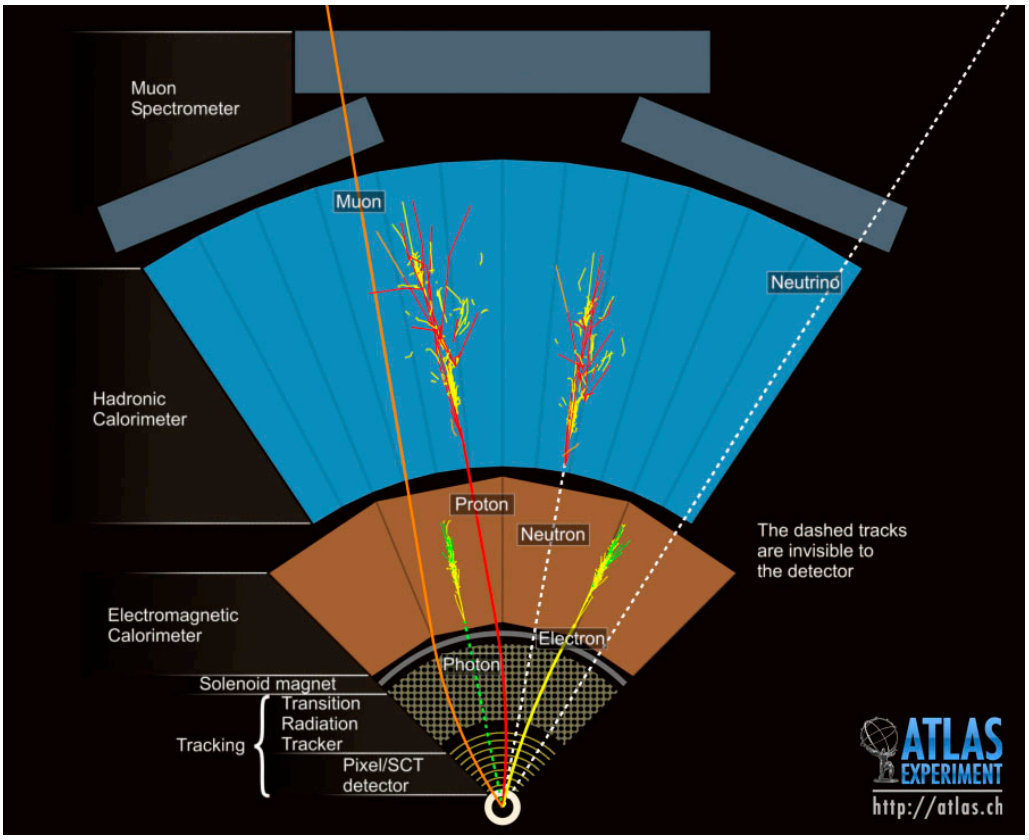

Figure 3.5: A cross section in the transverse plane of the ATLAS detector, showing the concentric sub-systems, and the interactions of different particles with these systems. Dashed lines are invisible to the detector. [20]

3.2.1 Magnet System

ATLAS uses its three magnet subsystems to bend charged particles in order to accurately measure their four-momentum by taking advantage of the Lorentz Force Law.

$$\mathbf{F} = q\mathbf{E} + q\mathbf{V} \times \mathbf{B} \tag{3.3}$$

By rearranging the Lorentz force, the momentum, p, for a given particle is obtained, relating to the magnetic field, B, and radius of curvature, r, by $\mathbf{p = qBr}$. The sub-systems are comprised of the central solenoid, the barrel toroid, and the end-cap toroid. The central solenoid completely encases the inner detector, and has a 2T field. The barrel and end-cap toroids both have 4T magnetic fields and sit around the calorimeter and in the end-caps respectively, as seen in Figure 3.6.

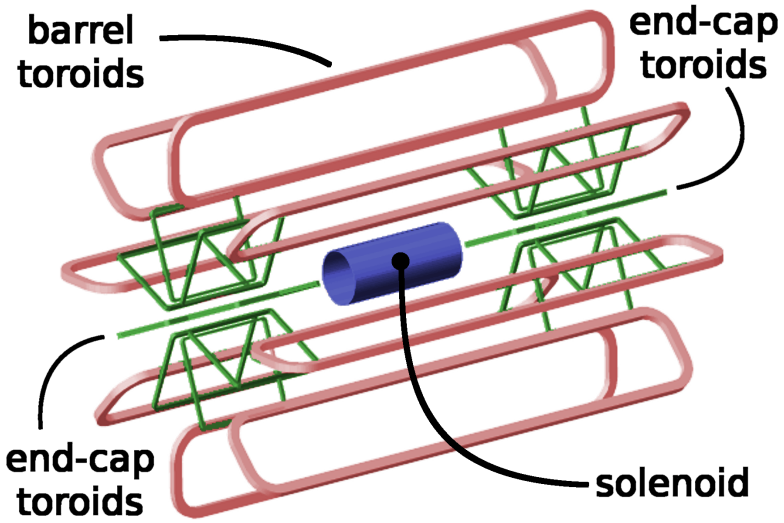

Figure 3.6: ATLAS magnet system schematic. [18]

3.2.2 Inner Detector

The Inner Detector is the most complex and sensitive of the detector sub-systems. Labelled in Figure 3.5 as "Tracking", it is the first part of ATLAS to see the decay products of the collisions. With a total diameter of 2.5 m, it is comprised of three different subsystems, all contained within the solenoid magnet, and is responsible for tracking the paths of charged particles. From closest to furthest from the beam line, the Inner Detector is comprised of the Pixel Detector, the Semi-Conductor Tracker (SCT), and the Transition Radiation Tracker (TRT).

The Pixel Detector is the innermost of the sub-detectors, and is responsible for providing the most precise position measurements. It covers a range of $|\eta| < 2.5$ in $R - \phi$ and z, and is made of high purity silicon. Typically, tracks cross three of the 50×400 μm^2 pixels, which across the detector make up some 80.4 million readout channels.

The Semi-Conductor Tracker (SCT) is made up of two sets of silicon strips; one in the z direction to measure in $R - \phi$, and petal-like radial strips in the end cap region. A track will generally cross the SCT eight times.

The Transition Radiation Tracker, comprised of straw drift tubes, supply both position measurements and particle identification. It operates only in $R - \phi$ but its 351,000 channels allow for up to 36 crossings of a track per event, so it is able to see tracks as they progress from $\eta = 0$ to $\eta = 2$, thus providing a high degree of precision in the transverse plane.

As the LHC increases the energy of proton collisions, more sensitive detectors with faster electronics need to be built to resolve different particle interactions. The upgrade of the Inner Tracker, ITk, and The University of Adelaide's role in these upgrades, will be presented in Chapter 4.

3.2.3 Calorimeters

ATLAS has two calorimeters; the electromagnetic calorimeter, and the hadronic calorimeter. The EM calorimeter measures the energy of electrons and photons as they interact with matter, in this case liquid Argon and lead. The hadronic calorimeter samples the energy of hadrons as they interact with the atomic nuclei of plastic scintillator tiles, in the case of the barrel, and liquid Argon in the end cap, and is used for jet reconstruction and $E_{\mathrm{T}}^{\mathrm{miss}}$ measurements. The calorimeters are designed to absorb most of the particles, and so they themselves act in part as radiation shielding for the muon system.

3.2.4 Muon Spectrometer

The outermost system of the ATLAS detector measures the momenta of muons. The muon spectrometer is made up of four different components; monitored drift tubes and cathode strip chambers measure the deviation of muons through the spectrometer under the influence of the magnetic field while resistive plate chambers and thin gap chambers are used for the trigger system. The barrel and end-cap magnet systems provide a field that is orthogonal to the muon trajectory, which reduces scattering and therefore improves precision.

3.2.5 Trigger System

With the order of 10^9 proton-proton collisions per second in the LHC, only small sample of these will produce events relevant to any specific analysis. To reduce the data to manageable levels, ATLAS uses a multi-level trigger system which selects events with specific energies or particle types. The L1 trigger searches for physics objects, such as photons, electrons, jets, high-p_T muons, and quantities such $E_{\mathrm{T}}^{\mathrm{miss}}$, and total transverse energy. It is a hardware trigger, and results from the muon spectrometer and calorimeters shape the Regions of Interest that are then passed to other electronic systems and higher level triggers. The higher level trigger is a software trigger, and uses the 2% of event data that has passed the L1 trigger to form events from all available detector data, before it is sent to offline processing and storage.

3.3 Object Definitions

Consistent metrics are needed so that physics objects can be defined in the detector. In general, they are split into leptons, jets, and the previously defined missing transverse energy, $E_{\mathrm{T}}^{\mathrm{miss}}$. Their energies are measured in electronVolts, eV.

3.3.1 Leptons

Real leptons must originate from a primary vertex that has at least two tracks, and each of these tracks must each have $p_T > 400$ MeV. For events with more than one primary vertex, the one with the largest p_T is used, and this is called the *leading lepton.*

Electrons

Electron candidates are identified in the calorimeter as an energy cluster, and must be reconstructed from a track observed in the Inner Detector. Using a predefined likelihood (LH) function, they are categorised as `LooseLH`, `MediumLH`, or `TightLH` which have identification efficiencies of 96%, 94%, and 88% respectively for an electron with $E_T > 15$ GeV [22] [23].

Muons

Muon candidates can be constructed by matching tracks from the Inner Detector to those in the Muon Spectrometer, and are reconstructed using one of four algorithms. Muon candidates $20 < p_T < 100$ GeV, are categorised into working points for identification; `Loose`, `Medium`, `Tight`, and `HighPt`, and have efficiencies of 98.1%, 96.1%, 91.8%, and 80.4% respectively [24].

Taus

Taus are not stable leptons, and so must be detected from their decay products. In the ATLAS detector, taus are reconstructed from hadronic decays [25], (rather than from QCD jets to reduce mis-identification), which present mostly as pions. Using the anti-k_T jet algorithm [26], events in the hadronic calorimeters with $p_T > 10$ GeV are used, again with `Tight`, `Medium`, and `Loose` working points with efficiencies of 60%, 45%, and 30% respectively for tau candidates with 40 GeV $< p_T <$ 100 GeV [27].

3.3.2 Jets

With the exception of the top quark, strongly interacting particles in the initial proton collision will decay. A *jet* is a cluster of a set of particles, which ATLAS identifies from particle tracks, and matches the tracks to strong activity in the

hadronic calorimeter [28]. There are a variety of clustering algorithms, but ATLAS uses the anti-k_T algorithm [26] with radius $\Delta R = 0.4$ for most analyses.

b-tagged jets

A b-jet is any jet that contains a b (or $\bar{b}$) quark. These are the result of the short-lived b quarks hadronising into a B-meson ($\bar{b}q$), and are described by a likelihood function which discriminates between jets with and without b objects [29].

3.4 Event Simulation

While it is important to correctly define and detect real events within particle physics, it is equally important to have robust theoretical models with which to compare event data. For this modelling, Monte Carlo (MC) generators are used. There are numerous generators, each of which use a different algorithm to generate a random set of events based on specific theoretical models.

3.4.1 Generators

Particles interact with themselves and each other in a variety of ways, at energies ranging from MeV to TeV. Generators are designed to model QCD scattering and perturbations. The *Leading Order* (LO) term in a perturbative expansion is the most important contribution to the model, with *Next-to-Leading Order* (NLO) being the next most important, and so on, with each subsequent order being more suppressed. The Matrix elements of these perturbations are calculated at least to LO, and often to NLO, using Parton Distribution Functions (PDFs). PDFs model the "probability to find partons (quarks and gluons) in a hadron as a function of the fraction x of the proton's momentum carried by the parton" [30]. The most commonly used generators for Standard Model interactions are Pythia [31], Herwig [32, 33], and MadGraph5 [34], and are specified for each individual analysis.

3.4.2 Weighting

Generators are designed to replicate specific observables observed in detectors, such as particle momentum and relative abundance. Event statistics can be increased, and uncertainties reduced, by weighting events. Usually, the whole sample is normalised to 1 fb^{-1} so that it can be scaled for each analysis, and conventionally the sum of weights is used, instead of the number of events. This in turn can lead to some events being assigned negative weights, which can cause problems in later modelling, as some algorithms are not designed to handle negatively weighted events, and studies must be performed to ensure their omission does not change the shape of kinematic variables.

Chapter 4

Inner Tracker Upgrades

The large volume of data produced by the LHC provides new and exciting challenges in the area of high-speed data acquisition in the ATLAS detector, and will yield a new set of challenges when the High-Luminosity LHC comes online in 2026. These challenges are being addressed by teams across the world, using a combination of software, hardware, and firmware, that is to be installed into the ATLAS detector during the Long Shutdown 3 in 2024–2026, shown in Figure 4.1. Presently, the University of Adelaide is involved with a test stand for the data acquisition (DAQ) for the Inner Tracker Pixel Detector, with the RD53A chipset. This work will enable future testing and studies of the Inner Tracker Pixel and Strip Modules as they are built, as well as providing a space to develop the supporting software and firmware for the data acquisition from these modules.

Statement of Contribution: The work done to set up and prepare the laboratory for the ITk modules has been largely performed by the author. While this work is done in collaboration with the ATLAS ITk team, it has been necessary to prepare an environment in which the work can be performed locally, including interfacing the proposed set up with pre-existing hardware capabilities. This has also resulted in a set of documentation for use by other local ATLAS members using our facilities.

4.1 HL-LHC

From 2026, the Large Hardon Collider will operate at an instantaneous luminosity of 7.5×10^{34} cm^{-2} s^{-1}, delivering over 200 proton collisions per bunch crossing [35]. In the decade after these upgrades, ATLAS aims to collect 4000 fb^{-1} data. This era is known as the High-Luminosity Large Hadron Collider, or HL-LHC. With this increase in data production and collection, new challenges are presented to both detector hardware and data acquisition methods. Physicists around the world are working to prototype, test, and produce new hardware and software solutions for the ATLAS collaboration.

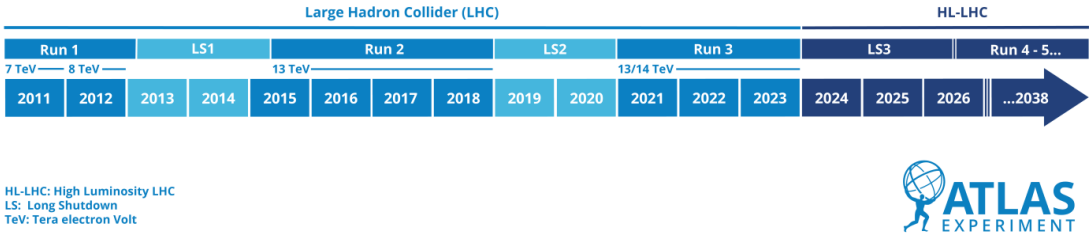

Figure 4.1: Upgrade and data collection timeline for the Large Hadron Collider. [36]

4.1.1 Overview of the Inner Tracker

As was discussed in Section 3.2.2, the Inner Tracker is the closest sub-detector system to the beam line, and therefore the most complex and has the highest sensor density. A diagram of the original Inner Detector is shown in Figure 4.2. The Pixel Detector, which is discussed in detail here, has over 80 million pixel units alone. This new system will be comprised of a Pixel Detector and a Strip Detector, and will take up the same volume as the current setup, so that the Transition Radiation Tracker will be replaced by these systems. Four barrel layers and six end cap petals at each end of the detector made of the Strip Modules will surround a five layer Pixel Detector. The ITk is designed to be a permanent fixture, and so will need to operate for 10 or more years at high efficiency, as only the two innermost Pixel layers will be able to be replaced at 2000 fb^{-1}. This calls for the materials to be radiation hard, as the 4000 fb^{-1} data will receive around 10 MGy of radiation [37]. Figure 4.3 shows a candidate layout of the Inner Tracker in $z - R$ space, where z is the distance along the beam line from the interaction point, and R is the radial distance from the interaction region. The Strip Modules are indicated in blue, and the Pixel Modules are in red.

4.1.2 Pixel detector

The Pixel Detector works by converting the charge deposited from particles passing through a silicon pixel into a digital value, and the time spent over a specific threshold value, Time over Threshold (ToT). This tracker will be made of high-purity silicon, and have precision tracking capabilities up to $|\eta| = 4$. The pixels themselves are either $50 \times 50\mu\text{m}^2$ or $25 \times 100\mu\text{m}^2$ and make up 10^4 hybrid modules of one to four pixels bonded to a silicon sensor. These modules are placed in three different configurations; parallel to the beamline in low η, tilted at an angle towards the beamline for medium η, and perpendicular to the beamline for high η.

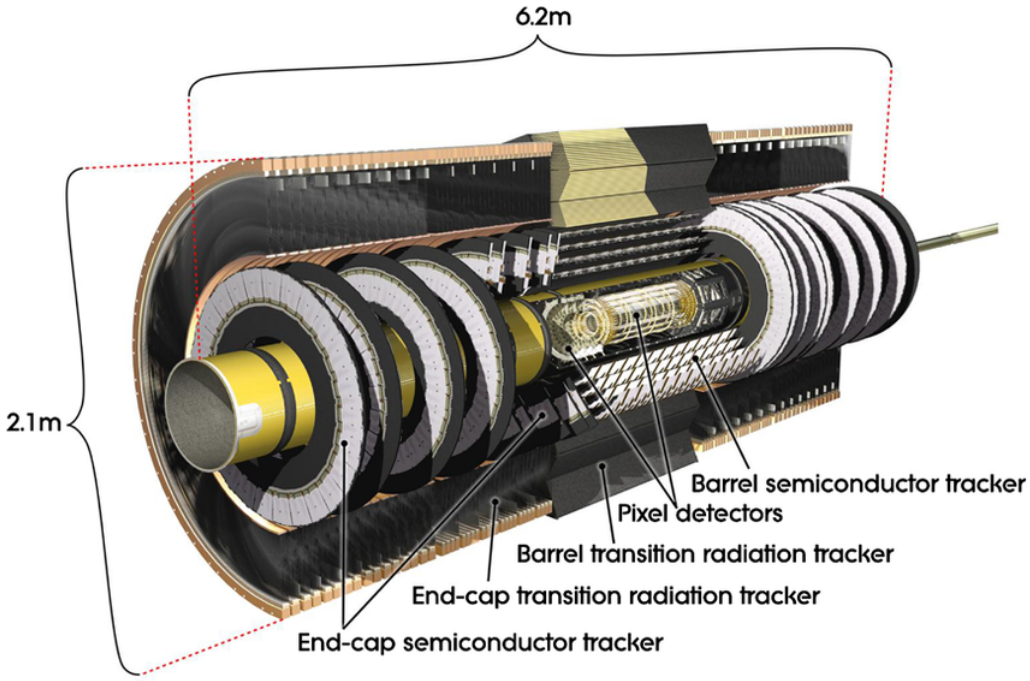

Figure 4.2: Detailed view of ATLAS' Inner Detector. [18]

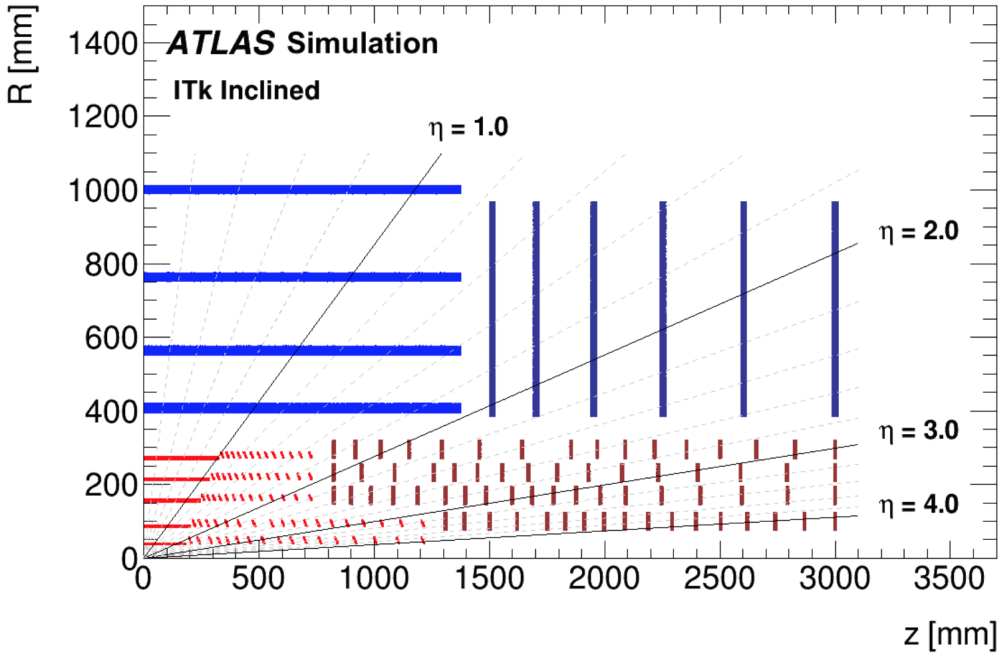

Figure 4.3: Schematic of the ITk layout with Strip Modules in blue, and the Pixel modules in red. [35]

4.2 Test Stand

The University of Adelaide is providing a test stand in which to try out some of the hardware that will be used for the ITk upgrades. Much of this set up involves providing a robust environment and documentation for the systems used and work performed, so that it is comparable to work done across the collaboration. Here, the work has revolved around the high-speed in-out (HSIO2) boards [38] with a mounted Reconfigurable Cluster Element (RCE) developed at the Stanford Linear Accelerator Complex (SLAC) in California, as well as working with the RD53A chipset [39] produced by the Lawrence Berkeley National Lab (LBNL). A schematic of the current setup and how it is interfaced with the Front End Boards (FEBs) is shown in Figure 4.4.

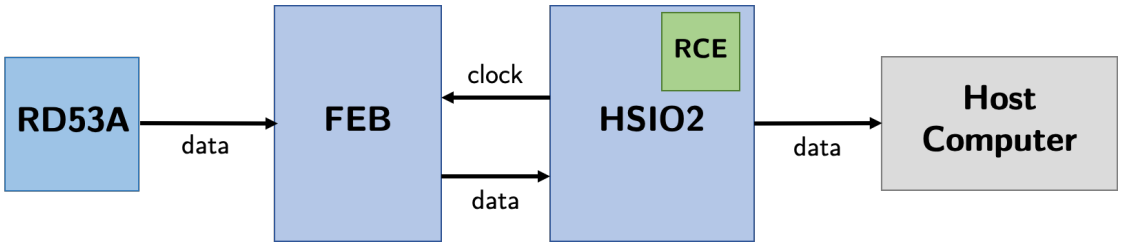

Figure 4.4: A simple schematic of the test stand setup at Adelaide University.

4.2.1 HSIO2 and RCE

The development board currently in use is the HSIO2, developed at SLAC, and shown in Figure 4.5. It is a simple interface platform comprised of a Rear Transition Module, a Reconfigurable Cluster Element, RCE, connectivity to Front-End (FE) electronics, and has the capacity to be parallelised with other HSIOs in an Advanced Telecommunications Computing Architecture (ATCA) crate. This board was designed to be a standardised system to provide buffering for the FEBs tested in the ITk upgrades. The small size of these modules allow for them to be placed in test beams and tested with realistic data before they are used in the ATLAS detector.

The HSIO2 hosts a Data Transition Module (DTM) which houses the RCE. The RCE is incredibly powerful as it allows for multiple pixel readouts, and up to four individually configurable modules are able to be hosted per board. These RCEs are able to be individually accessed and reconfigured, so that if there is a new firmware update, or an issue with one RCE, it can be rectified with software and firmware on the fly, without interrupting the operation of the other Pixel Modules or ITk as a whole. With such a complex setup, this configurability is a powerful tool that would allow the ATLAS detector to continue operation should a problem occur mid-run.

Clock synchronisation is one of the most important aspects of data acquisition. It is imperative that all components of the ATLAS detector are perfectly synchronised with not just each other, but the LHC as a whole, to enable precision tracking. The

RCE allows the combination of several parallel data streams to be combined and sent through a 10 GB/s ethernet uplink.

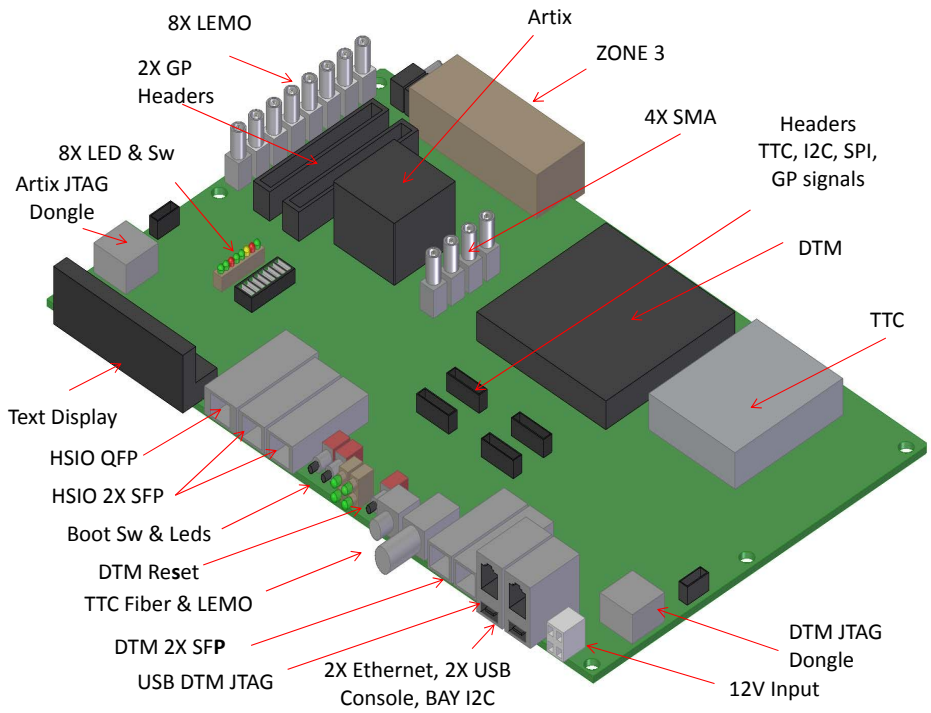

Figure 4.5: Diagram of the High-Speed In-Out board showing connectivity ports. [38]

4.2.2 The RD53A Chip

The RD53 Collaboration is a team from both both the ATLAS and CMS (Compact Muon Solenoid) experiments who are designing and producing pixel readout chips for the upgrades at the HL-LHC. Their current focus is developing a test chip, the RD53A, which will enable many institutions to test the primary features of the pixel front end, such as irradiation, geometry, bonding to other modules, and high-speed data I/O. The FE hardware is shown in Figure 4.6 and the RD53A chip in Figure 4.7. The RD53A connects to one of the eight Pixel Module connections on the FEB, and the FEB to the HSIO2.

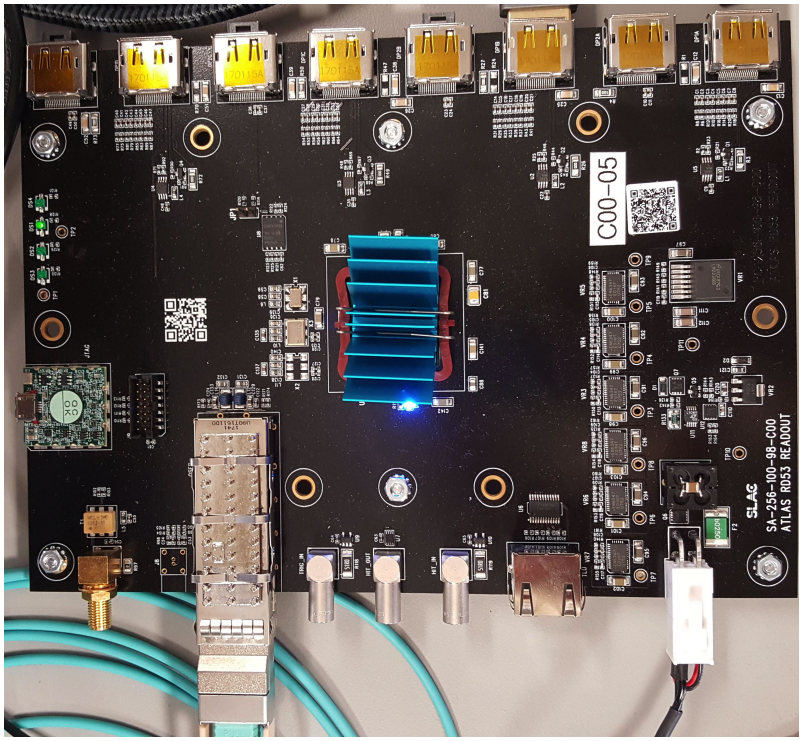

Figure 4.6: A Front End Board showing connectivity for up to eight Pixel Modules.

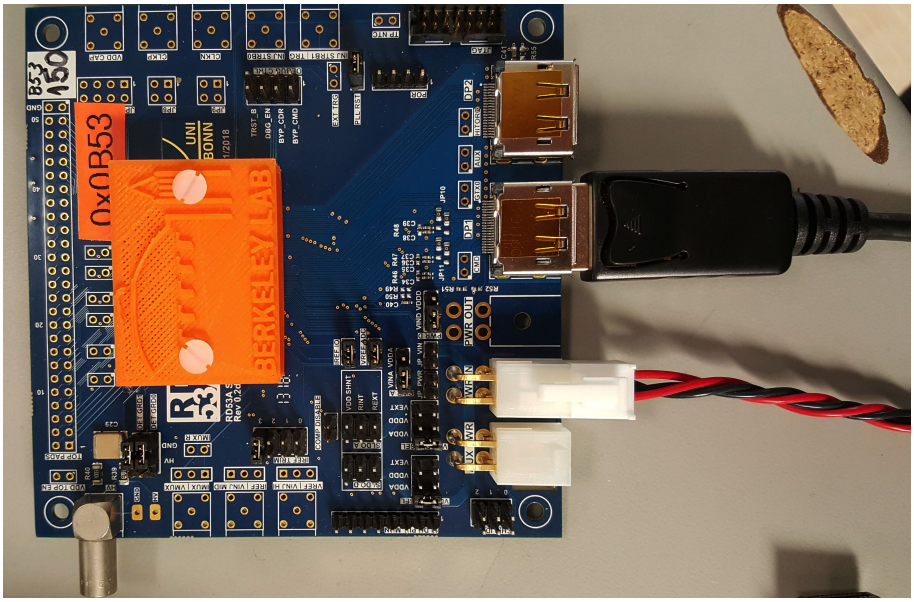

Figure 4.7: The RD53A chip.

4.2.3 YARR

The software currently in use for testing and debugging the hardware is Yet Another Rapid Readout, or YARR [40]. This software is a flexible platform that integrates both Strip and Pixel modules, and allows for many different FE hardware configurations. It also hosts the RD53A emulator and has been especially useful for running ToT scans and for debugging connectivity issues before FE hardware is acquired.

4.2.4 Current Status

Presently, the Adelaide test stand is able to connect the host computer to the RCE and HSIO2 to load and update firmware. The HSIO2 is able to be interfaced with the ATCA crate to allow for parallelisation of multiple boards and RCEs, which are able to be accessed and reset individually. The RD53A emulator runs dummy scans and interfaces well with the host computer. The hardware setup was trialled in May 2019 at SLAC and LBNL through a remote connection and with a number of different configurations in preparation for FE hardware when it is available. Documentation is being produced for this specific setup and for the tests being performed. Once Pixel Modules are produced in the coming years, they will be able to be tested here. The test bench at the University of Adelaide is designed to provide a robust and repeatable experimental environment for the testing of ITk modules.

Chapter 5

The Standard Model Four Top Analysis

The Standard Model predicts the production of events containing four top quarks, $t\bar{t}t\bar{t}$. Until the advent of the LHC, it has been impossible to create this process. As such, to date it has not been observed due to its complex decay structure and low cross section, currently predicted to be $\sigma_{t\bar{t}t\bar{t}} = 11.97^{+18\%}_{-21\%}$ fb [41]. The aim of this analysis is to be able to extract a statistically prevalent signal strength of the four top process from the background processes. The signal strength acts as a measure of signal presence in data, with $\mu = 0$ representing a background-only hypothesis, and $\mu = 1$ being the background with a Standard Model $t\bar{t}t\bar{t}$ process, currently measured to be $\mu_{t\bar{t}t\bar{t}} = 1.08$ [41]. Deviations from a value of unity would indicate that a different cross section would better model the process. This result will be considered significant if the measurement fluctuates more than 3σ from the results in [41].

The four top channel is a promising place to look for new, or Beyond Standard Model (BSM) physics, as the top quark has near-unity coupling to the Higgs boson, and it is theorised that the Higgs couples to BSM candidate particles.

The $t\bar{t}t\bar{t}$ analysis is being performed with Boosted Decision Trees and Multivariate Analysis Packages to extract a signal strength, and this chapter details some of the processes used to extract the $t\bar{t}t\bar{t}$ signal in the same-sign and multi-lepton regions (SSML), using 139 fb^{-1} data collected from Run II of the ATLAS detector during 2015–2018. Figure 5.1 shows the production diagrams for four top quarks.

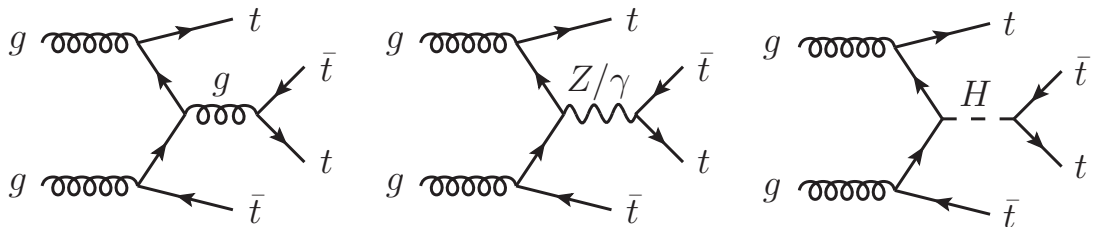

Figure 5.1: Feynmann diagrams showing the production of $t\bar{t}t\bar{t}$ at leading order in the Standard Model [42].

5.1 Top Quark Properties

The top quark was first detected at Fermilab in 1995 [43] and has a mass of 173 GeV [4]. It the heaviest elementary particle, and has the shortest lifespan at 5×10^{-26} s. The unique properties of the top quark allow for an exploration of new and exciting physics phenomena, such as particles beyond the Standard Model, and rare Standard Model processes. These searches are able to be performed due to the existence of hadron colliders.

In proton-proton colliders such as at the LHC, top quarks can be produced in pairs, from mainly $q\bar{q} \rightarrow t\bar{t}$ and $gg \rightarrow t\bar{t}$ at leading order. At the LHC, the dominant production mechanism for $t\bar{t}$ is gg. The current cross section for $t\bar{t}$ at the LHC is $\sigma_{t\bar{t}} = 830.4$ pb [44]. From the CKM Matrix, (Equation 2.1), it is seen that $|V_{tb}| = 0.999$. Therefore, the top quark decays to a bottom quark almost exclusively, and it is the only decay mode considered here. This decay produces a W^+ boson, as seen in Figure 5.2, and is the same for a $\bar{t}$ quark, with charges of the other particles reversed.

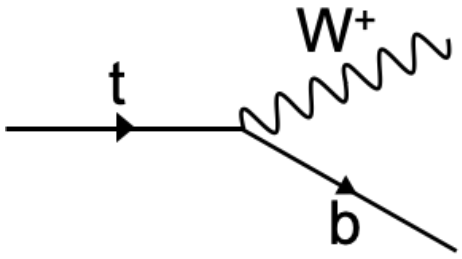

Figure 5.2: The top quark is considered to decay to a bottom quark and W^+ boson.

5.1.1 W Boson Properties

As it is the W boson that mediates the top decay, it is the W whose decay products are of particular interest, especially when forming the signal region for the $t\bar{t}t\bar{t}$ analysis. The W boson decays either *hadronically* to a quark anti-quark ($q\bar{q}'$) pair, or *leptonically* to a lepton neutrino ($l\nu$) pair, as shown in Figure 5.3. These decays are experimentally measured to occur at different rates, both for single $W^\pm$ decays, and for states with W^+W^- pairs, such as those coming from a $t\bar{t}$ pair like those produced in the $t\bar{t}t\bar{t}$ analysis. The decays and associated branching fractions of single and paired W bosons are summarised in Table 5.1 and the final states of top-anti-top pairs via the W are summarised in Table 5.2.

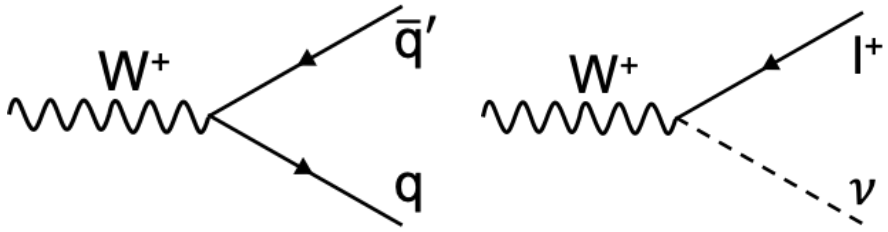

(a) $W \to q\bar{q}'$ (b) $W \to l\nu$

Figure 5.3: W boson decay modes.

Table 5.1: Decays and associated branching fractions of the W boson. [4]

Decay Mode			Branching Ratio
W^+	$\to$	$q\bar{q}'$	$67.41 \pm 0.27\%$
W^+	$\to$	$l^+\nu$	$32.59 \pm 0.40\%$

Table 5.2: $t\bar{t}$ decay modes. [4]

$t\bar{t}$ Decay Modes					Branching Ratio	Decay Type
$t\bar{t}$	$\to$	$W^+bW^-\bar{b}$	$\to$	$q\bar{q}'bq''\bar{q}'''\bar{b}$	$45.7 \pm 0.4\%$	fully hadronic
$t\bar{t}$	$\to$	$W^+bW^-\bar{b}$	$\to$	$q\bar{q}'bl^-\bar{\nu}_l\bar{b} + q''\bar{q}'''bl^+\nu_l\bar{b}$	$43.8 \pm 0.7\%$	semi-leptonic
$t\bar{t}$	$\to$	$W^+bW^-\bar{b}$	$\to$	$l'^+\nu_{l'}bl^-\bar{\nu}_l\bar{b}$	$10.5 \pm 0.3\%$	fully leptonic

Currently, $t\bar{t}t\bar{t}$ production is being explored by the ATLAS Collaboration in two main channels, 1LOS, and SSML, which are one lepton, and a pair of opposite sign leptons, and a pair of same-sign leptons or three leptons, respectively. Here, leptons refer only to electrons and muons, but may include those that are produced from a tau decay. Figure 5.4 shows the branching ratios of the possible final states for four top quarks. Only the SSML channel is considered in this thesis.

As discussed in Section 5.1, top quarks decay into bottom quarks and W-bosons, both of which hadronise into an array of jets, visible objects such as leptons, and invisible objects such as neutrinos. The SSML analysis channel monopolises on regions of phase space with low background event contamination, even though the branching ratio is only 12.1% of the total W decay.

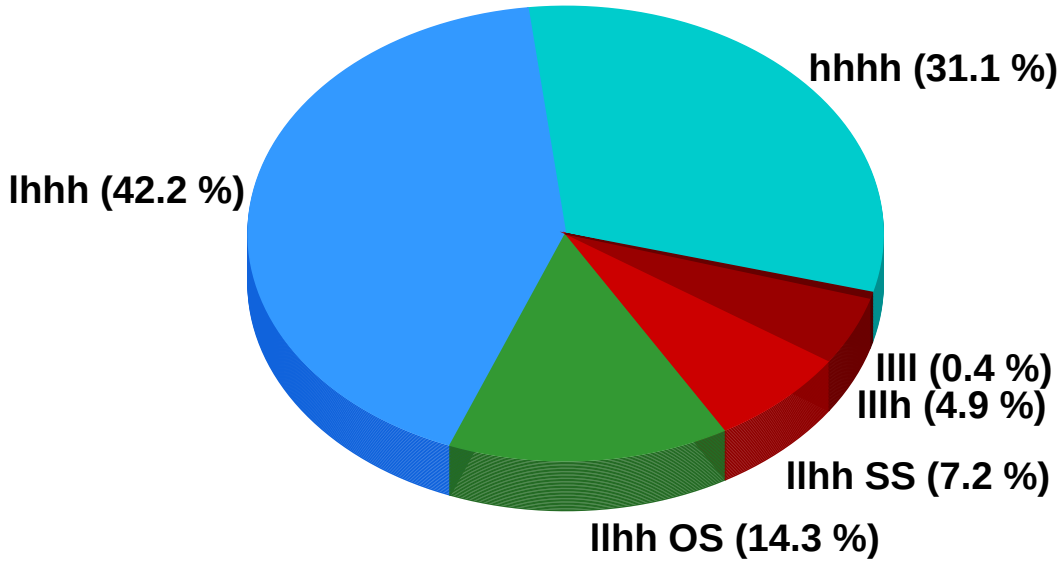

Figure 5.4: Branching ratio for four W bosons, where l is an electron or muon, h is a hadronic decay, SS is same-sign leptons, and OS is opposite-sign leptons. [45]

5.2 Object and region definitions

Before events are categorised into sub-channels, they must first pass a pre-selection. For the SSML region, this selection includes the requirement that there must be at least two same-sign leptons, each with $p_T >$ 28 GeV, and one or more b-tagged jets. In the multi-lepton events and di-electron same-sign events, the combined mass $m_{\ell\ell}$ of these leptons must fall outside of a Z-mass window, $81 < m_{\ell\ell} < 101$ GeV.

The physics objects considered in this $t\bar{t}t\bar{t}$ measurement are electrons, muons, jets, b-jets and missing transverse momentum. These objects are discussed in detail in the following section, and are summarised in Table 5.3. The channels are shown in Figures 5.5 and 5.6.

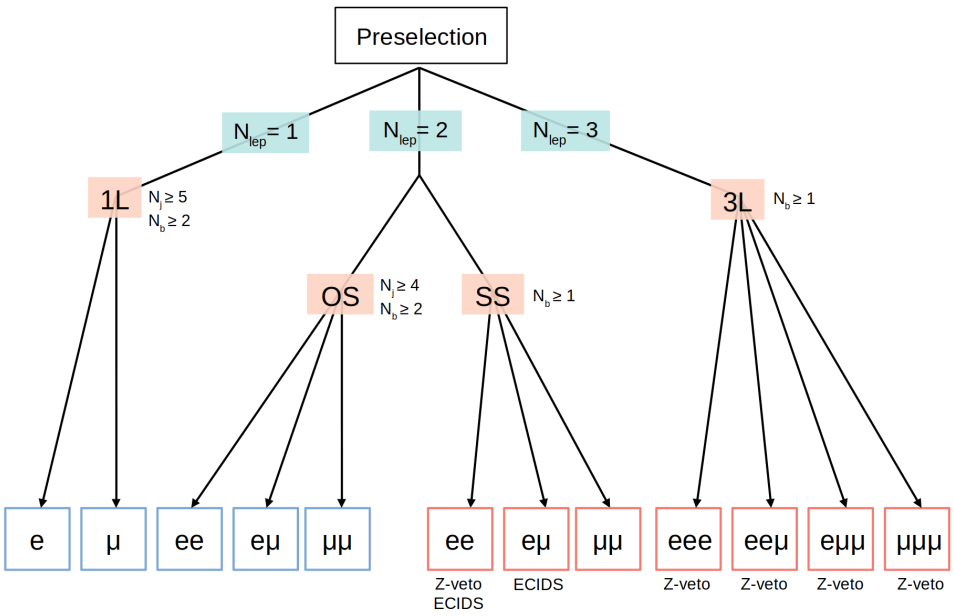

Figure 5.5: Events are split by lepton multiplicity, then further categorised into channels by lepton charge, and then sub-categorised by flavour. [45]

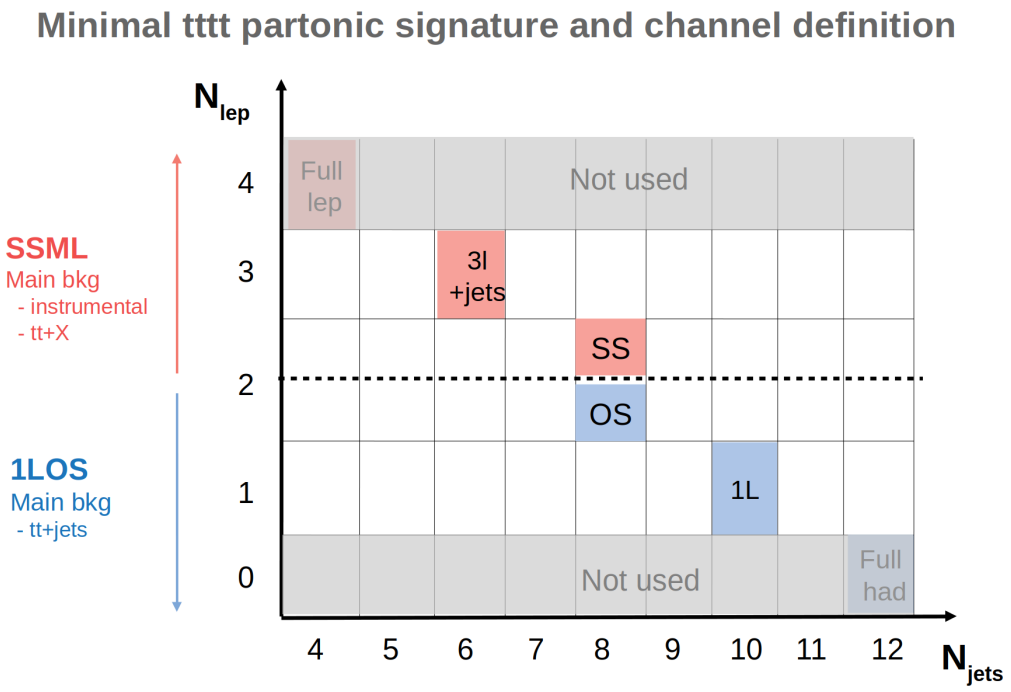

Figure 5.6: Channel definition for the Standard Model Four Top analysis. The 1LOS analysis is not considered in this work. [45]

Table 5.3: Summary of object identification and definitions.

	Electrons		Muons		Jets	b-jets
	loose	tight	loose	tight		
p_T[GeV]	> 10 or > 28		> 10 or > 28		> 25	> 25
$\|\eta\|$	< 1.37 or $1.52 - 2.47$		< 2.5		< 2.5	< 2.5
ID quality	mediumLH ECIDS (ee, $e\mu$)	tightLH ECIDS (ee, $e\mu$)	medium		cleaning + JVT	MV2c10 70% o r 77%
Isolation	none	FCTight	none	FixedCutTightTrackOnly		
Track vertex :						
$- \|d_0/\sigma_{d_0}\|$	< 5		< 3			
$- \|z_0 \sin\theta\|$ [mm]	< 0.5		< 0.5			

5.2.1 Electrons

The Egamma Combined Performance (CP) group recommends a likelihood-based electron identification which implements cut-based methods to improve background rejection [46]. There are five working points which are supported for likelihood-based (LH) electrons [47], of which the `TightLH` identification (88% efficiency) is used here, with an additional requirement on the electron isolation corresponding to the `FCTight` isolation working point (WP) [48]. In the region ($1.37 < |\eta| < 1.52$), electrons are rejected to reduce the contribution from non-prompt and fake electrons due to detector design in the liquid Argon calorimeter, known as the LAr crack region. Electron candidates satisfying $p_T > 28$ GeV and $|\eta| < 2.47$ (except the LAr crack region veto) are selected. Scale factors are then applied to the Monte Carlo simulation to correct for efficiency differences between data and Monte Carlo events.

The $e^{\pm}e^{\pm}$ and $e^{\pm}\mu^{\pm}$ channels are sensitive to charge mis-identification, as events often contain a high-p_T electron, which presents as near-straight track, making charge identification more difficult. A Boosted Decision Tree discriminant, ECIDS [49], is used to average the charge from multiple calorimeter hits, and obtain the correct polarity. For the `TightLH` working point, the ECIDS operates at 98.05%.

5.2.2 Muons

The Muon Combined Performance Working group (MCP) [50] supports five working point effeciencies for muons, and in this analysis they are required to pass the `Medium` quality (96.1% efficiency), with $p_T > 28$ GeV, and $|\eta| < 2.5$. Additionally, muons must pass the `FixedCutTightTrackOnly` isolation working point [48]. The MCP-recommended standard selection for the longitudinal and transverse impact parameters are applied. Similarly to electron candidates, for muons the associated scale factors for identification and isolation are applied as multiplicative factors to the Monte Carlo simulation event weights.

5.2.3 Jets

Jets are reconstructed using the anti-k_t algorithm [26] with a radius of $R = 0.4$ using topological calorimeter clusters [51]. To suppress jets which originate from pile-up collisions, the JetVertexTagger (JVT) [52] is applied to the selected jets [53]. Only jet candidates satisfying $p_T > 25$ GeV and $|\eta| < 2.5$ are selected.

b-jet tagging

As previously discussed, top quarks always decay to produce bottom quarks, and so *b*-jets are especially pertinent to this analysis. The multivariate MV2c10 algorithm [54] is used to identify jets which originate from a *b*-hadron. The *b*-jet selection is made on an efficiency of 77% for the SSML channel, however to use the full *b*-tagging information of an event, each jet is given a pseudo-continuous *b*-tagging score that defines if the jet passes the *b*-tagging operating points of 85%, 77%, 70% and 60%, giving respectively a score of five, four, three and two, or if the jet does not pass any of the previous working points, one. It is this tagging score that is used as a variable in the analysis.

5.2.4 Missing Transverse Momentum

The missing transverse momentum vector $\mathbf{p}_{\mathrm{T}}^{\mathrm{miss}}$, with magnitude $E_{\mathrm{T}}^{\mathrm{miss}}$ is used to define candidate neutrinos, which cannot be directly measured in the ATLAS detector. Here,

$$\mathbf{p}_{\mathrm{T}}^{\mathrm{miss}} = -\left(\mathbf{p}_{\mathrm{T}}^{\mathrm{Ele}} + \mathbf{p}_{\mathrm{T}}^{\mathrm{Muon}} + \mathbf{p}_{\mathrm{T}}^{\mathrm{Jet}} + \mathbf{p}_{\mathrm{T}}^{\mathrm{SoftTerm}}\right), \tag{5.1}$$

where $\mathbf{p}_{\mathrm{T}}^{\mathrm{SoftTerm}}$ arises from tracks not associated to any reconstructed object.

5.2.5 Overlap removal

A procedure called Overlap Removal is used to avoid double counting in final state objects. The `Loose` definitions for electrons and muons are applied, which have efficiencies of 96% and 98.1% respectively. An algorithm is used to solve ambiguities where the same detector information is used for multiple particle candidates. This algorithm uses the `BoostedSlidingDRMu` option [55]:

- An electron candidate track overlapping with another electron is removed.
- In the calorimeter, a muon sharing a track with an electron is removed.
- Electron candidates which share a track with muon candidates are removed.
- If ΔR between a jet and an electron is smaller than 0.2, the jet is dropped. In cases of multiple jets fulfilling this criteria, only the closest jet (with respect to ΔR) is removed.

- A jet with fewer than three tracks associated to it which is located within $\Delta R < 0.2$ of a muon is removed.
- A jet with fewer than three tracks associated to it is removed if it has a muon inner-detector track matched to it.
- The muon is removed if the distance between a jet and the muon is $\Delta R < 0.4$.
- The muon is removed if the distiance between a remaining jet and the muon is $\Delta R < 0.4 + 10\,\text{GeV}/p_{\text{T}\mu}$, with $p_{\text{T}\mu}$ being the transverse momentum of the muon.

The AnalysisTop software (tag 21.2.75) is used for the final results in the $t\bar{t}t\bar{t}$ analysis. The AnalysisTop software will not be discussed further, only referenced here for completeness. It is only important to note that this software is a dedicated package, written for the purposes of Top physics at ATLAS, and was kept consistent throughout the analysis.

5.3 Defining the Four Top Signal

The analysis uses three types of region to look for events containing four top quarks; the Signal Region (SR), Control Region (CR), and Validation Region (VR). These regions allow data and Monte Carlo events to be compared, to ensure correct modelling for the backgrounds present. The Signal region is presented separately to the Control and Validation Regions, which will be discussed as part of Section 5.5. The multiplicity and kinematic restraints on these objects are known as *cuts*. These regions are summarised in Table 5.4, where H_T is measured in GeV, and $M_{ee}@ConvV$ and $M_{ee}@PV$ is the dielectron mass from the conversion vertex, or primary vertex, respectively. Further definitions are provided in the following sections.

Table 5.4: Summary of Signal, Control, and Validation Regions for the SSML channel. H_T takes units of GeV. These regions and objects are defined in the following sections.

Region	Channel	N_j	N_b	Other Requirements	Fitted Variable
SR	SS+3L	≥ 6	≥ 2	$H_T > 500$	BDT
CRttbarCO	SSee || SSmm	$4 \leq N_j < 6$	≥ 1	$0 < M_{ee}@ConvV < 0.1$ $200 < H_T < 500$	M_{ee}@PV
CR1b3Le	eee || eem		$= 1$	$100 < H_T < 250$	Leading p_T(l)
CR1b3Lm	emm || mmm		$= 1$	$100 < H_T < 250$	Leading p_T(l)
CRttW2L	SSee || SSmm	$4 \leq N_j$	≥ 2	$M_{ee} < 0$ or $M_{ee} > 0.1$, $\lvert\eta(e)\rvert < 1.5$ for $N_b = 2$, $H_T > 500$ or $N_j < 6$ for $N_b \geq 3$, $H_T < 500$	$\Sigma p_T(l)$
CRlowBDT	SS+3L	≥ 6	≥ 2	$H_T > 500$, $BDT < -0.2$	BDT
VR ttZ	3L, failed Z veto	≥ 6	≥ 2	$H_T > 500$	counting

5.3.1 Signal Region

The *Signal Region* (SR) is a subset of phase space in which the events of interest, in this case, four top quarks, are most likely to be found. In order to prevent a biased optimisation of the analysis, this region is *blinded* until all backgrounds and signal Monte Carlo are adequately modelled. For the SSML region, events are required to have two same-sign leptons, or three leptons, at least six jets, of which at least two are b-tagged, and that the scalar sum of these objects' transverse momenta, H_T, is at least 500 GeV, as shown in Figure 5.7. The method for extracting the four top signal using Boosted Decision Trees (BDTs) and the results obtained are discussed at length in Section 5.4.

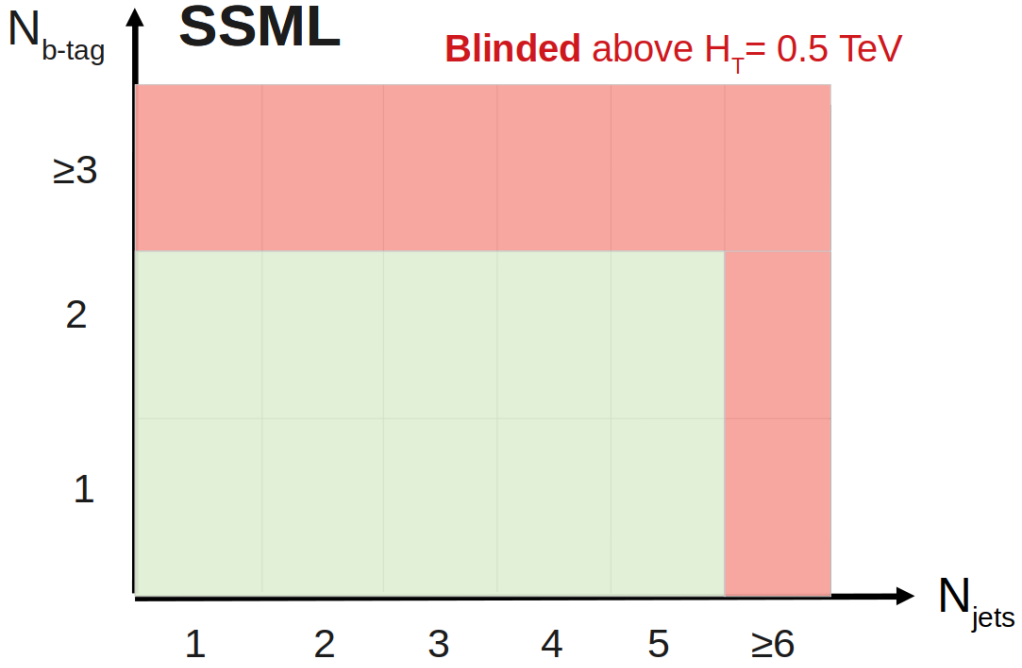

Figure 5.7: The Signal Region is blinded above 500 GeV. [45]

5.4 Multivariate analysis

There is often no one 'right way' to perform a physics analysis, especially if it involves complex final states, or events with a small cross section. One way to extract a signal strength is with a Multivariate Analysis, in this case performed with *ROOT*'s Toolkit for Multivariate Analysis (`TMVA`), using Boosted Decision Trees (BDTs). Performing a multivariate analysis allows the analysis to be performed on a number of different physics variables simultaneously, particularly for those which might be correlated. This method has proved especially successful in the $t\bar{t}t\bar{t}$ SSML analysis, as the Signal Region suffers from low statistics, which can be overcome through training the model on Monte Carlo, which can be scaled up to have many more events.

Statement of Contribution: The author's main contribution to the SM Four Top analysis has been in the optimising and testing of the Boosted Decision Trees. These tests were done by changing the input parameters, and manually checking the ROC integral and overtraining plots for each combination. These tests were also performed with an iterative removal process of the variables to produce a final list of variables and parameters over which to run the full analysis to optimise the signal strength obtained.

5.4.1 Boosted Decision Trees

A decision tree is a way of dividing phase space using multiple classifications, or binary operations. Decision trees can also undergo *boosting*, when different algorithms are applied to the same classifications to improve the performance and stability of the final tree. The $t\bar{t}t\bar{t}$ analysis uses a *binary classifier* to divide events into Signal and Background regions, and additionally employs a bagging technique, where trees are repeatedly sampled to minimise statistical fluctuations. This is important for regions with low statistics, such as the $t\bar{t}t\bar{t}$ signal, and multi-lepton backgrounds. These trees are weighted and recombined to give a single tree as a final result. The trained events need to be tested against the expected outcome, and thus the Monte Carlo events are divided into two groups, training and testing, based on their event number, odd or even, which enables the studies to be replicated and compared using full event statistics. Event counts show that this method of splitting yields a less than 1% difference between odd and even groups. The events trained through the BDT are then plotted against their untrained partners to determine if the BDT is performing correctly.

First, 20% of the events are set aside and are not used in any optimisation, which ensures that there is no bias when checking training and testing events. The remaining 80% are split by odd or even `eventNumber`, which gives two equal and orthogonal sections of the sample that are easily reproducible for every training and testing, as shown in Figure 5.8.

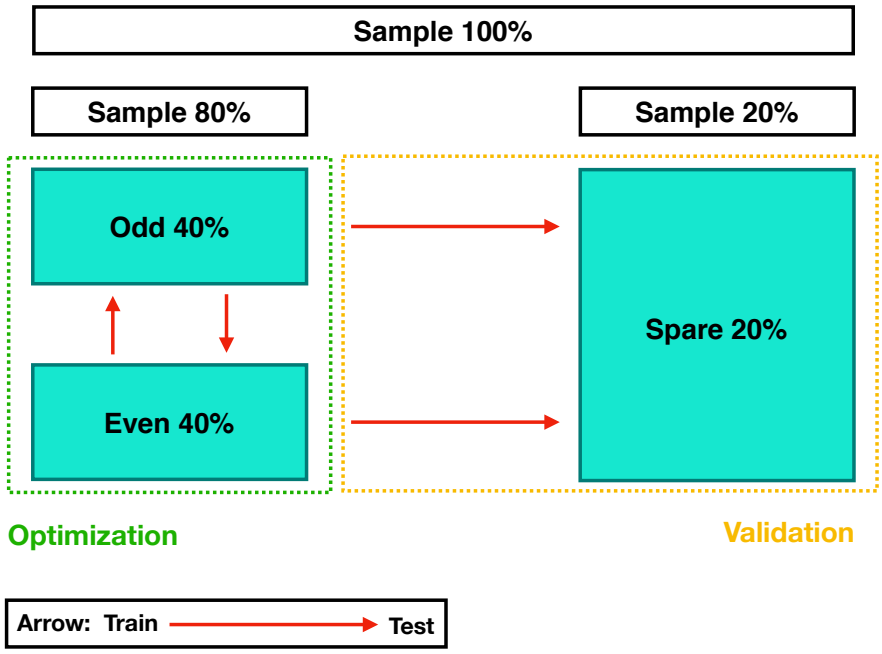

Figure 5.8: Overview of BDT sample training. [45]

The BDT then undergoes *training* and *testing* on each of the 40% sections of events. During *training*, the truth information is provided to the BDT so that it can learn which events are signal and which are background. This is done to the odd and even samples separately, which generates a weighted discriminant variable between -1 and +1, with -1 being most background-like, and +1 being most signal-like. This variable is then applied to the other sample in the *testing* step. If the training was performed on the odd sample, it will be tested on the even sample, and vice versa. The outputs of this step are plotted and must be checked manually for poor modelling. It is, however, possible that any errors introduced in these steps will go unnoticed across the 80%, so the training is then *validated* on the remaining 20% that was not used previously, to check the performance on a sample never used in the BDT.

Table 5.5 shows the signal selection criteria that are used to select events on which to train the BDT. Here, the SSML signal region is used with only MC events in the $t\bar{t}t\bar{t}$ sample. Any Data/MC comparisons used to validate the BDT are done in the $BDT \leq -0.2$ region, which should contain mostly background events, in order to keep the Signal Region blinded.

Table 5.5: BDT event selection.

Region/Variable	$H_{\mathrm{T}}^{\mathrm{all}}$ [GeV]	N_{j}	N_b (MV2c10@77%)	Leptons
BDT	> 500	≥ 6	≥ 2	SS2L || 3L

While the BDT could be trained on all variables in the nTuple, the analysis would then involve the systematic errors on all variables, reducing precision of the training

for no additional gain. Additionally, only a few variables are useful for studying the separation between background and signal, and some variables are highly correlated.

There are two kinds of discriminating factor taken into account when selecting variables for use in a multivariate analysis; a variable's separation, and its ranking. *Separation* describes the power a variable has to distinguish between signal and background particle distribution functions. The separation is zero for identical PDFs, and one for shapes with no overlap. Figure 5.9 shows a comparison of the b-tagging score, which has good background (red) and signal (blue) separation, with the leading lepton p_T, which shows no separation. Separation is modelled by

$$\langle S^2 \rangle = \frac{1}{2} \int \frac{(\hat{y}_S(y) - \hat{y}_B(y))^2}{\hat{y}_S(y) + \hat{y}_B(y)} dy \tag{5.2}$$

for some variable y, for signal S and background B [56]. For this analysis, the separation of variables is used in addition to the knowledge of a particle's kinematic behaviour. For example, it is known that a $t\bar{t}t\bar{t}$ event will have at least four b-tagged jets, whereas a single top process would only have one, but this is not so obvious for other kinematics, such as lepton and jet distance, so the separation plots are used to make an initial selection.

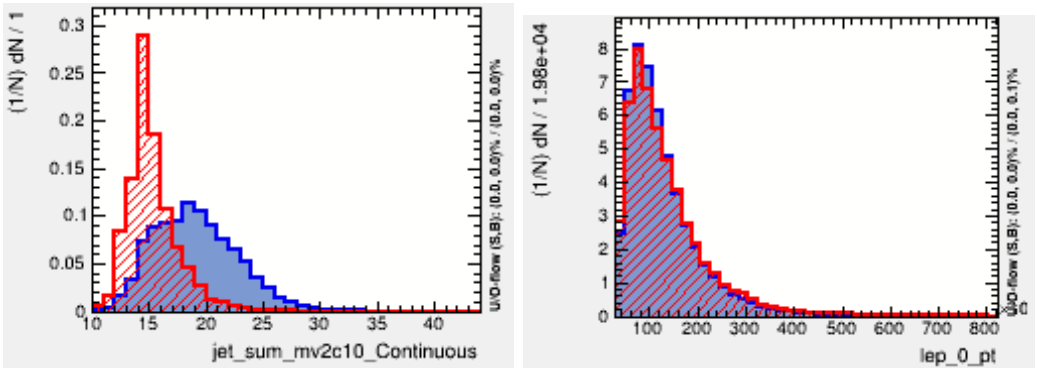

Figure 5.9: Comparison of variables that have good signal and background separation (b-tagging score, left) with one that does not (leading lepton p_T, right).

The *ranking* of a variable indicates how often it is used to split the binary tree nodes, weighted by the square of the separation gain this yields. It is more mathematically robust than separation, as it gives a numerical outcome that can be directly compared between all variables.

Gradient Boosting

Gradient boosting is an algorithm that is robust in the presence of outlier or mislabelled data points, which is useful for low statistics regions, and so it is used in the $t\bar{t}t\bar{t}$ analysis. The `TMVA GradientBoost` minimises a binomial log-likelihood loss of

$$L(F, y) = \ln(1 + e^{-2F(x)y}) \tag{5.3}$$

to classify signal and background events for variable y [56]. This works best on small trees and are therefore much less likely to be overtrained. This robustness can be further increased with the use of a Shrinkage parameter, which controls the weight assigned to each individual tree, and is the rate at which the model learns. A small shrinkage, in the range of 0.1-0.3, increases the number of trees grown, therefore improving the accuracy of the prediction as the residuals in the model are smaller.

ROC Curves

A ROC curve, short for Receiver Operating Characteristic, is a measure of how well a signal can be measured against a single background, or set of backgrounds. It is impossible to separate signal events completely from background processes, but careful event selection criteria, as was discussed in 5.2, is key in identifying events that come from the production from four top quarks, as opposed to those that do not, but may have similar physics signatures. The integral of the ROC curve – a value between 0 and 1 – measures how much signal is correctly obtained, calculated by Equations 5.4 and 5.5. This is represented graphically by a curve showing Signal vs Background Rejection, and the variable of interest obtained is the Area Under Curve (AUC) or integral, shown in Figure 5.10. An integral close to 1 indicates a well-modelled BDT outcome. It is important to note, however, that this curve and integral alone cannot determine whether the model has been trained correctly, just that it seems to perform well, which can lead to Type I and Type II statistical errors, as shown in Table 5.6. Once the signal and background overlays have been checked for overtraining outcomes, it is the ROC integral that determines how well the BDT performs.

$$\varepsilon_{sig} = \frac{\text{N.Events classified as signal}}{\text{N.Events truly signal}} \begin{cases} 1 & \text{All signal correctly obtained (best)} \\ 0 & \text{No signal correctly obtained (worst)} \end{cases} \tag{5.4}$$

$$\varepsilon_{bkg} = \frac{\text{N.Events classified as signal}}{\text{N.Events truly background}} \begin{cases} 1 & \text{All background wrongly classified as signal (worst)} \\ 0 & \text{No background wrongly classified as signal (best)} \end{cases} \tag{5.5}$$

Table 5.6: Types of statistical errors possible.

True \ Classified	Signal	Background
Signal	True Positive	Type-II Error (False Negative)
Background	Type-I Error (False Positive)	True Negative

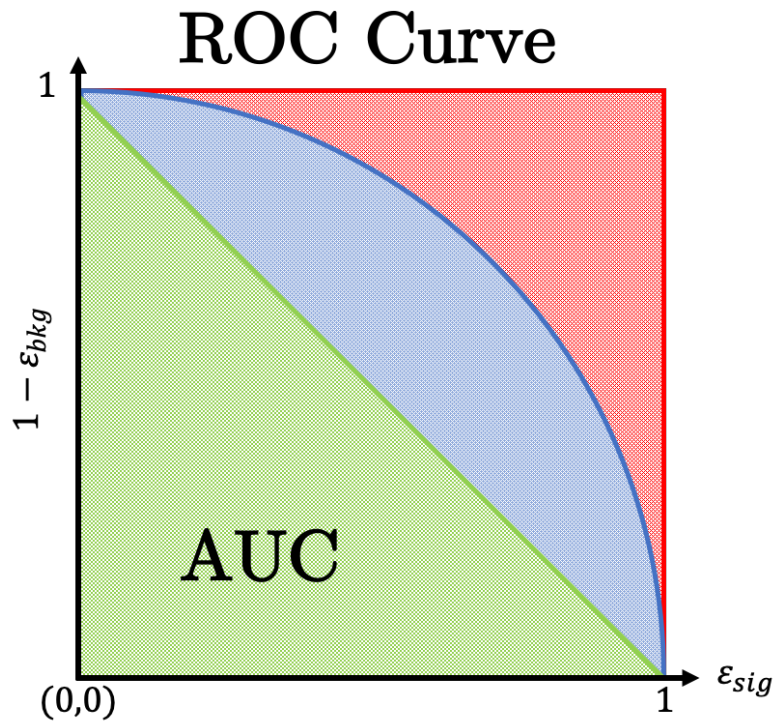

Figure 5.10: Sample ROC Curve showing an Area Under Curve (AUC) of 0.50 (green), 0.79 (blue), and 1 (red).

5.4.2 Optimising the BDT

The `TMVA` package has a set of default parameters, which are fine-tuned for each analysis to improve the signal to background ratio. The tuning of these parameters is determined by the value of the AUC, and the appearance of over- or under-training in the output, as shown in Figure 5.11. These parameters are then iteratively changed, while checking training plots and AUCs, until an optimal value is reached. Along with these parameters, the variables included in the BDT are also removed iteratively, to check their impact on the overall fit. The parameters used in this optimisation are

- Maximum Depth (Max.D.): Number of maximum split BDT nodes allowed
- Number of Cuts (nCuts): Number of grid points in variable range used in finding optimal cut in node splitting
- Minimum event fraction (nMin%): Minimum percentage of events in leaf required to split
- Shrinkage: Weight of individual trees (learning rate)
- Bagging: Random sampling fraction size, which includes resampling
- Number of trees (nTrees): Number of trees grown during the iteration

The default parameters used in TMVA are summarised in Table 5.8, which gives a ROC integral of 0.851, as shown in Figure 5.12.

Using the output list of variables from the BDT testing, and removing the lowest ranked variable out of any two that had a more than 70% correlation, a list of the most important variables is summarised in Table 5.7. The variables are listed by their ranking, according to the output of the `TMVA` ranking variable.

Table 5.7: Variables used in the initial optimisations of the BDT. The Rank is output of the `TMVA` ranking variable.

Rank	Variable	Description
1	$\Sigma \mathrm{w}_{\mathrm{MV2c10}}$	Sum of MV2c10 pseudo-continuous b-tagging score over all jets
2	$\mathrm{p}_{\mathrm{T}}^{\ell_0}$	Transverse momentum of leading lepton
3	$\mathrm{E}_{\mathrm{T}}^{\mathrm{miss}}$	Missing transverse energy
4	$\Delta\mathrm{R}(\ell,\ell)_{\mathrm{min}}$	The minimum distance between any lepton pair
5	$\mathrm{p}_{\mathrm{T}}^{jet_5}$	Transverse momentum of 6th leading jet
6	$\Delta\mathrm{R}(\ell,b)_{\mathrm{max}}$	The maximum distance between leptons and b-tagged jets
7	$\mathrm{H}_{\mathrm{T}}^{\text{no lead jet}}$	Scalar sum of all lepton and jet p_T except leading jet
8	$\Sigma\Delta\mathrm{R}(\ell,\ell)_{\mathrm{min}}$	Sum of the distance between leading and sub-leading leptons in SS or leading, sub-leading and third-leading leptons in 3ℓ
9	$\Delta\phi(\ell_0, j_0)$	The transverse angle between leading lepton and jet
10	$\mathrm{p}_{\mathrm{T}}^{jet_0}$	Transverse momentum of leading jet
11	$\Delta\mathrm{R}(j,b)_{\mathrm{min}}$	The minimum distance between b-tagged jets and jets
12	$\Delta\mathrm{R}(\ell,j)_{\mathrm{min}}$	The minimum distance between leptons and jets
13	$\mathrm{p}_{\mathrm{T}}^{b-jet_0}$	Transverse momentum of leading b-tagged jet
14	$\Delta\mathrm{R}(\ell,b)_{\mathrm{min}}$	The minimum distance between leptons and b-tagged jets
15	$\mathrm{p}_{\mathrm{T}}^{\ell_1}$	Transverse momentum of sub-leading lepton
16	$\mathrm{p}_{\mathrm{T}}^{jet_2}$	Transverse momentum of third-leading jet
17	$\mathrm{p}_{\mathrm{T}}^{jet_1}$	Transverse momentum of sub-leading jet
18	nJets	Number of jets
19	nleps	Number of leptons
20	$\mathrm{p}_{\mathrm{T}}^{\ell_2}$	Transverse momentum of third-leading lepton

Table 5.8: Default parameters for multivariate analyses in TMVA.

Tree	Depth	nmin	Shrink	Bagging	ROC
800	6	3	0.1	0.7	0.851

Figure 5.11 shows that while the high (signal) end of the BDT is well trained, the low end, especially between -1.0 and -0.6 is over-trained. This is represented by the trained points having a much larger value than the untrained (test) curve. The model would benefit from optimisation as these parameters assume too many background events are present in the sample.

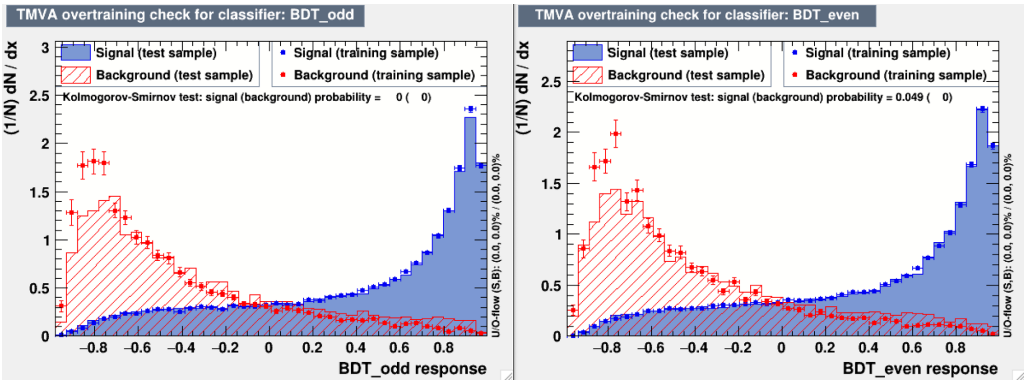

Figure 5.11: Training response for BDT trained on odd events (left) and even events (right) with the default parameters given in Table 5.8.

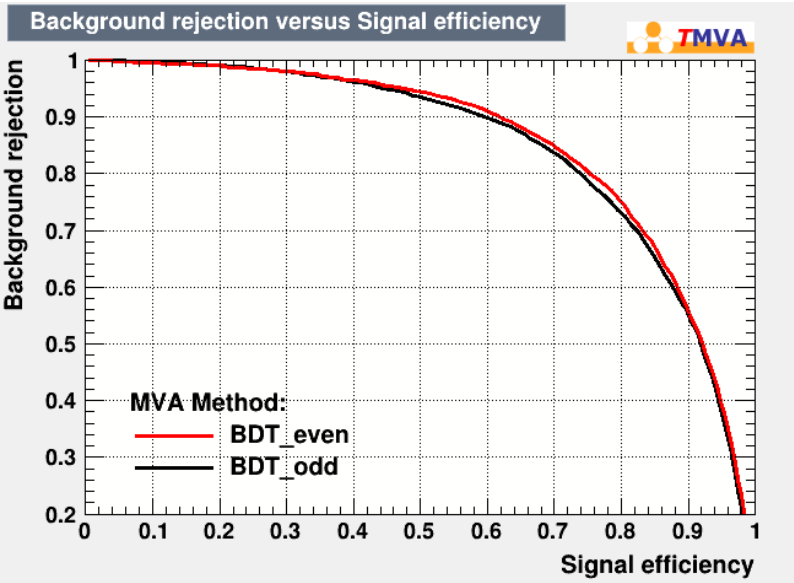

Figure 5.12: ROC Curve for default BDT hyperparameters given in Table 5.8 with an integral value of 0.851.

To begin the optimisation process, each parameter was incremented up and down to determine the effect on the ROC curve and possible over-training. Each of these hyperparameters is detailed in Table 5.9. It can be seen that, while the fluctuations are small, the Shrink parameter has the largest effect on the ROC curve, and lowering it produces a better result. This was confirmed by the over-training plots in Figure 5.13, which showed a much better performance of the training points, where they are overlaid closely to the shape of the curve. As a further check, the Shrink parameter was left at 0.1 and the other variables incremented as before, none of which showed any improvement to either the over-training plot or the ROC integral.

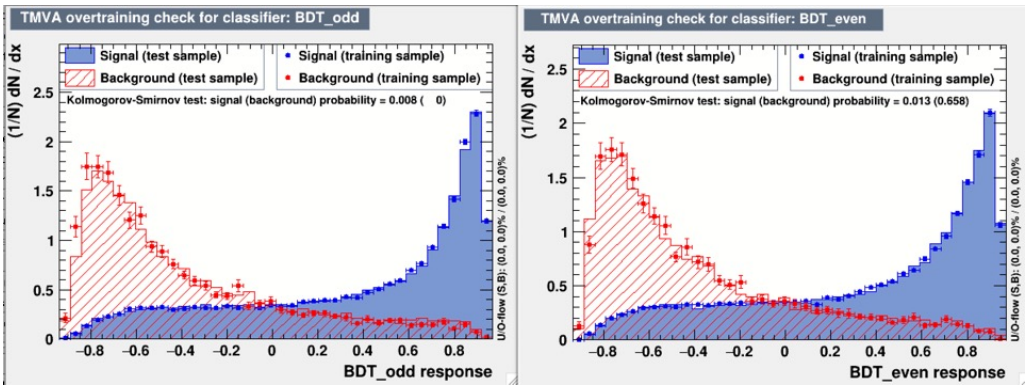

Figure 5.13: Lowering the Shrink parameter to its minimum (0.01) gives good comparison between testing and training for both odd (left) and even (right) events.

Table 5.9: Parameters used for optimising the Boosted Decision Trees. The first row is the default configuration, and then each parameter is iterated up and down for the subsequent pairs of rows, in order of parameter from left to right.

Tree	Depth	nmin	Shrink	Bagging	ROC
800	6	3	0.1	0.7	0.851
1000	6	3	0.1	0.7	0.849
600	6	3	0.1	0.7	0.850
800	5	3	0.1	0.7	0.850
800	7	3	0.1	0.7	0.849
800	6	2	0.1	0.7	0.849
800	6	4	0.1	0.7	0.849
800	6	3	0.05	0.7	0.853
800	6	3	0.2	0.7	0.844
800	6	3	0.1	0.6	0.849
800	6	3	0.1	0.8	0.849

Iterative Removal

Once the hyperparameters for the BDT have been set, and the variables ranked, it is possible to remove variables that do not contribute to the signal using the process of *iterative removal*. In this process, the last variable in the ranked list is removed, and the BDT repeated. If the ROC integral decreases, the variable is kept. No change, or an increase in the performance of the BDT will see the variable removed. This process was repeated until the lowest-ranking variable was still able to provide performance improvements. Sometimes it is also necessary to remove variables for which there are not enough statistics, such as the `njets`. This variable has a high systematic error and it was decided that the increase in error on the final fit was not worth the small gain in signal strength achieved with the BDT. The final list of variables is summarised in Table 5.10.

Table 5.10: Final list of variables used in the BDT. The Rank is output of the TMVA ranking variable.

Rank	Variable	Description
1	$\Sigma w_{\mathrm{MV2c10}}$	Sum of MV2c10 pseudo-continuous b-tagging score over all jets
2	$p_T^{\ell_0}$	Transverse momentum of leading lepton
3	E_T^{miss}	Missing transverse energy
4	$\Delta R(\ell,\ell)_{\mathrm{min}}$	The minimum distance between any lepton pair
5	$p_T^{jet_5}$	Transverse momentum of 6th leading jet
6	$\Delta R(\ell,b)_{\mathrm{max}}$	The maximum distance between leptons and b-tagged jets
7	$H_T^{\text{no lead jet}}$	Scalar sum of all lepton and jet p_T except leading jet
8	$\Sigma\Delta R(\ell,\ell)_{\mathrm{min}}$	Sum of the distance between leading and sub-leading leptons in SS or leading, sub-leading and third-leading leptons in 3ℓ
10	$p_T^{jet_0}$	Transverse momentum of leading jet
11	$\Delta R(j,b)_{\mathrm{min}}$	The minimum distance between b-tagged jets and jets
13	$p_T^{b-jet_0}$	Transverse momentum of leading b-tagged jet
17	$p_T^{jet_1}$	Transverse momentum of sub-leading jet

5.4.3 Negative Weight Treatment

Monte Carlo events are generated, and then weighted according to the theoretical expectations of the Standard Model to coincide with previous experimental measurements, as was discussed in Section 3.4. In some generators, this can be done by giving events a negative weight. It was uncertain how the TMVA package would behave with these negative weights, and so a study was performed to check the shape and relative event yield of the $t\bar{t}t\bar{t}$ signal both with and without negative weights. TMVA has an option to include or ignore negatively weighted events, and ignores them by default.

Only the NLO sample of the $t\bar{t}t\bar{t}$ signal MC contained negatively weighted events, and so the two studies performed were comparing LO and NLO, and NLO with and without negative weights. This is especially important because of the possible kinematic shape differences in the NLO signal sample as compared to the LO sample.

The kinematic distributions for the most affected variables were compared for the LO sample, the NLO sample, and the NLO sample for only positively weighted MC events, labelled NLO ≥ 0. These comparison plots of variables in Table 5.10 can be seen in Figures 5.14 to 5.16, showing both event yields, and an NLO/LO ratio with sum-square weighted errors. The plots for all variables show that there is a negligible difference in the number of normalised events between the three samples. The ratio plots further demonstrate that the kinematic shapes agree between samples within uncertainties.

It was ultimately concluded that using only the leading order sample for the $t\bar{t}t\bar{t}$ signal in the testing and training of the BDT was sufficient, and that these shape differences could be accounted for within systematic uncertainties.

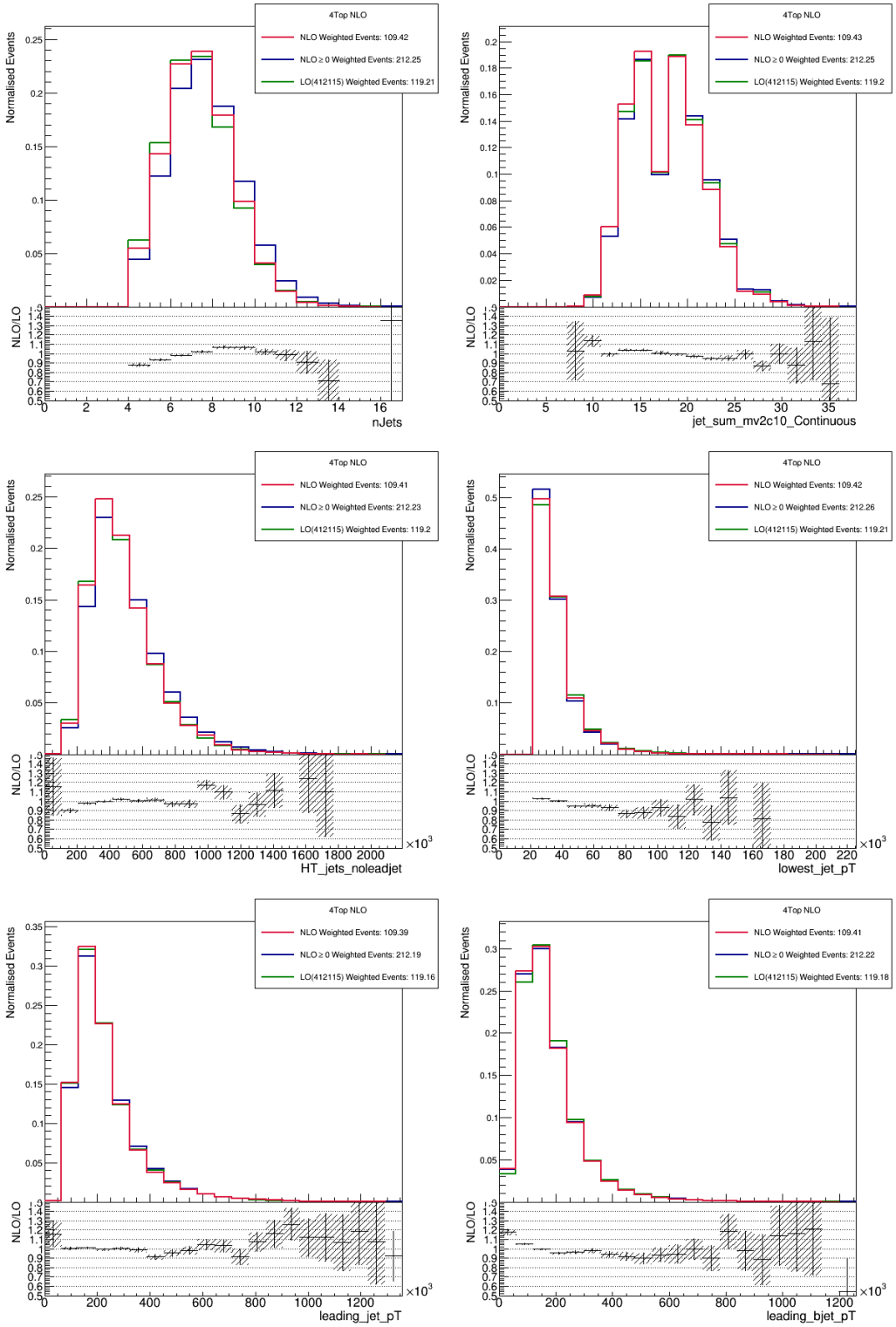

Figure 5.14: Negative weight studies for variables in Table 5.10.

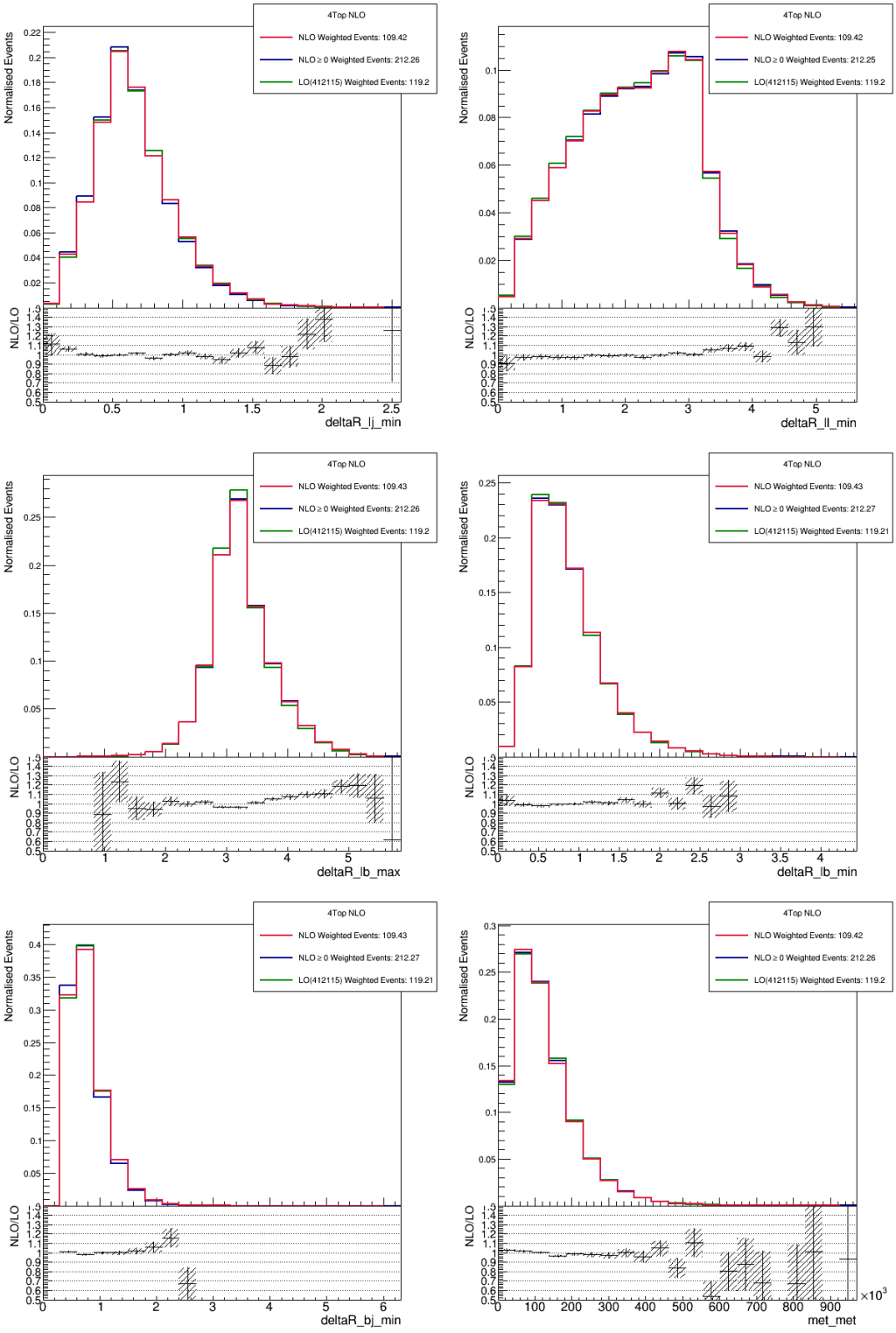

Figure 5.15: Negative weight studies for variables in Table 5.10.

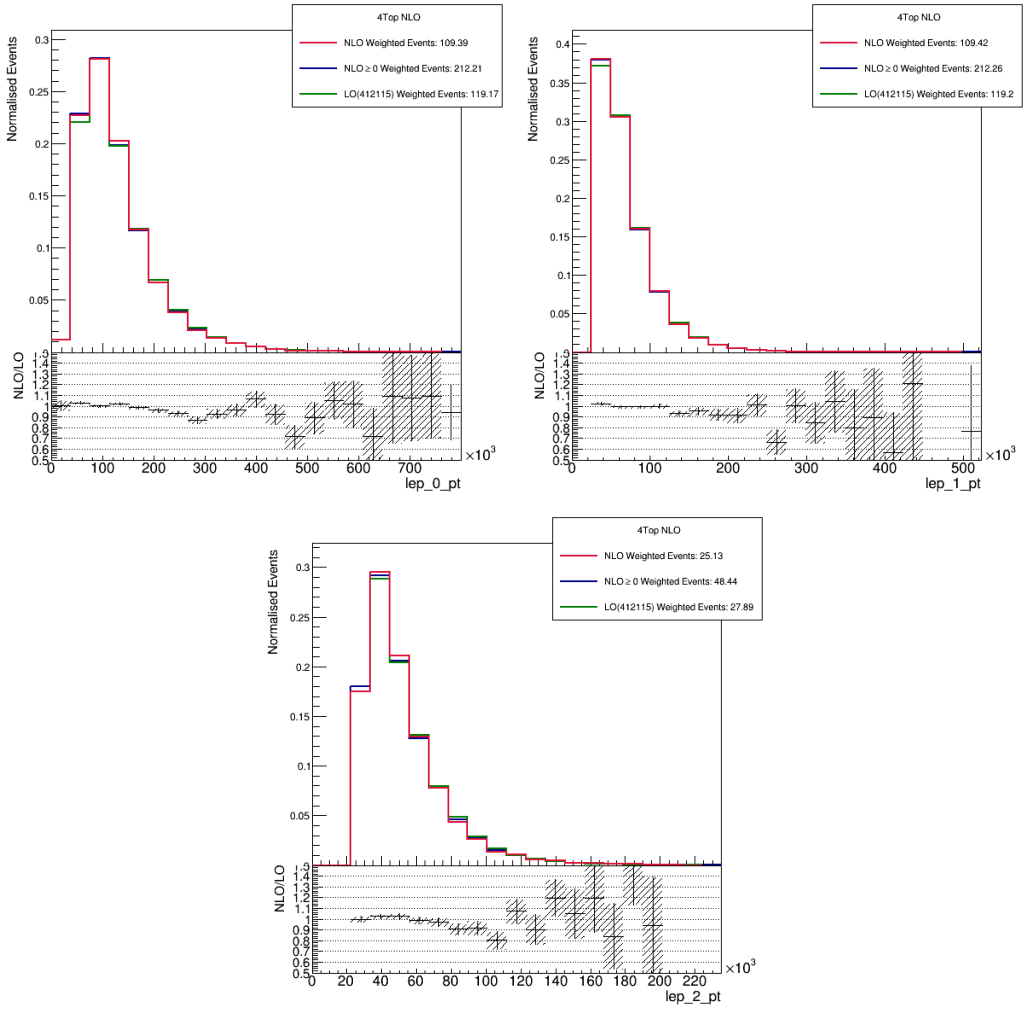

Figure 5.16: Negative weight studies for variables in Table 5.10.

5.5 Major Backgrounds

There are two kinds of backgrounds that need to be addressed in this analysis; physics backgrounds, and detector effects. Physics backgrounds arise from processes with similar final states and kinematics to the $t\bar{t}t\bar{t}$ signal, and need to be accurately modelled to ensure they are not confounded with signal events. In this analysis, the physics backgrounds are mainly comprised of $t\bar{t}W$ and $t\bar{t}Z$ events. Detector effects arise due to the interaction of particles with the detector, and how they are measured. These backgrounds involve mainly charge mis-identification of electrons in the same-sign channel. Background studies are performed with Monte Carlo modelling, and checked using Control and Validation regions. Good agreement between data and MC in the post-fit plots indicate that backgrounds have been well modelled. Once the preselection of events has been performed, the backgrounds are divided into three main categories; $t\bar{t}X$, QmisID, and Fakes/$\gamma*$.

- $t\bar{t}X$: Events where leptons originate from W or Z decays, such as $t\bar{t}W$, $t\bar{t}Z$, $t\bar{t}H$, or diboson or triboson events with associated jets. These backgrounds are modelled with Monte Carlo simulations.

- QmisID: Events (in the same-sign channel only) with an opposite-sign dilepton pair where one of the lepton charges has been mis-reconstructed. This is especially prevalent in higher p_{T} electrons, which have a straighter track through the inner detector, and is deemed negligible for muons.

- Fakes/$\gamma*$: Events which contain a lepton which is non-prompt, i.e. those that come from heavy flavour decays, such as c or b quarks, or a fake electron coming from quark or gluon jets.

5.5.1 Control Region

Control Regions (CR) are areas of phase space enriched in background events. There are five orthogonal CRs in the SSML channel, each focussing on a particular set of background events. Data in these regions is overlaid on Monte Carlo, and events are then scaled to obtain a *Normalisation Factor* (NF) for each background;

- `NF` $t\bar{t}W$: normalisation factor applied to events where leptons originate from $t\bar{t}W$ decays

- `NF HF e`: normalisation factor applied to events with one non-prompt electron from heavy flavour decay

- `NF HF` μ: normalisation factor applied to events with one non-prompt muon from heavy flavour decay

- `NF CO`: normalisation factor applied to events with one non-prompt electron coming from photon material conversion

- NF γ^*: normalisation factor applied to events with one non-prompt electron coming from (photon) γ^* conversion, as defined in 5.5 Fakes/$\gamma*$.

The Control Regions used to obtain these normalisation factors are;

- CRttbarCO: two same sign electron or electron-muon with a low value of the invariant mass between the electron and a close-by track pointing to the conversion vertex (which needs to have been found), at least four jets but less than six, at least one b-jet and $200 < H_T < 500$ GeV. The fitted variable is the invariant mass of the two leptons, and constrains both NF CO and NF γ^*
- CR1b3Le: three leptons with at least two electrons, exactly one b-jet and $100 < H_T < 250$ GeV. The leading lepton p_{T} is fit to constrain NF HF e
- CR1b3Lm: three leptons with at least two muons, exactly one b-jet and $100 < H_T < 250$ GeV. Again, the leading lepton p_{T} is used to constrain NF HF μ
- CRttW2L: two same sign electron-muon or muons, at least four jets, at least two b-jets, with the absolute value of the electron pseudo-rapidity less than 1.5, with SR blinding cuts applied. Fitting the sum of the lepton p_{T} constrains NF $t\bar{t}W$.
- CRlowBDT: the low part of the multivariate discriminant (BDT $\leq$ -0.2) used to extract the signal, with at least six jets and at least two b-jets. This region is included to check Data/MC agreement in the background tail of the multivariate fit. The BDT is described in detail in Section 5.4.1.

The background studies yielded the Normalisation Factors in Table 5.11, and these results are used in the backgrounds for the Multivariate Analysis. Results of these fits are presented in Figures 5.17 and 5.18, which show good modelling and agreement between data and MC for fitted variables after fitting. Fits in this analysis are performed using the Top Related Experiment Fitter (TRExFitter) [57]. This package provides a profile likelihood fit on multiple regions in multiple bins, and generates pre- and post-fit plots and tables, as well as expected significance of the signal.

Table 5.11: Fitted values of the 5 Normalisation Factors from the Control Region studies.

Parameter	NF $t\bar{t}W$	NF CO	NF γ^*	NF HF e	NF HF μ
Value ($\pm$ Stat.+Syst.)	1.66 $\pm$ 0.27	1.75 $\pm$ 0.53	0.88 $\pm$ 0.37	1.14 $\pm$ 0.40	0.94 $\pm$ 0.31

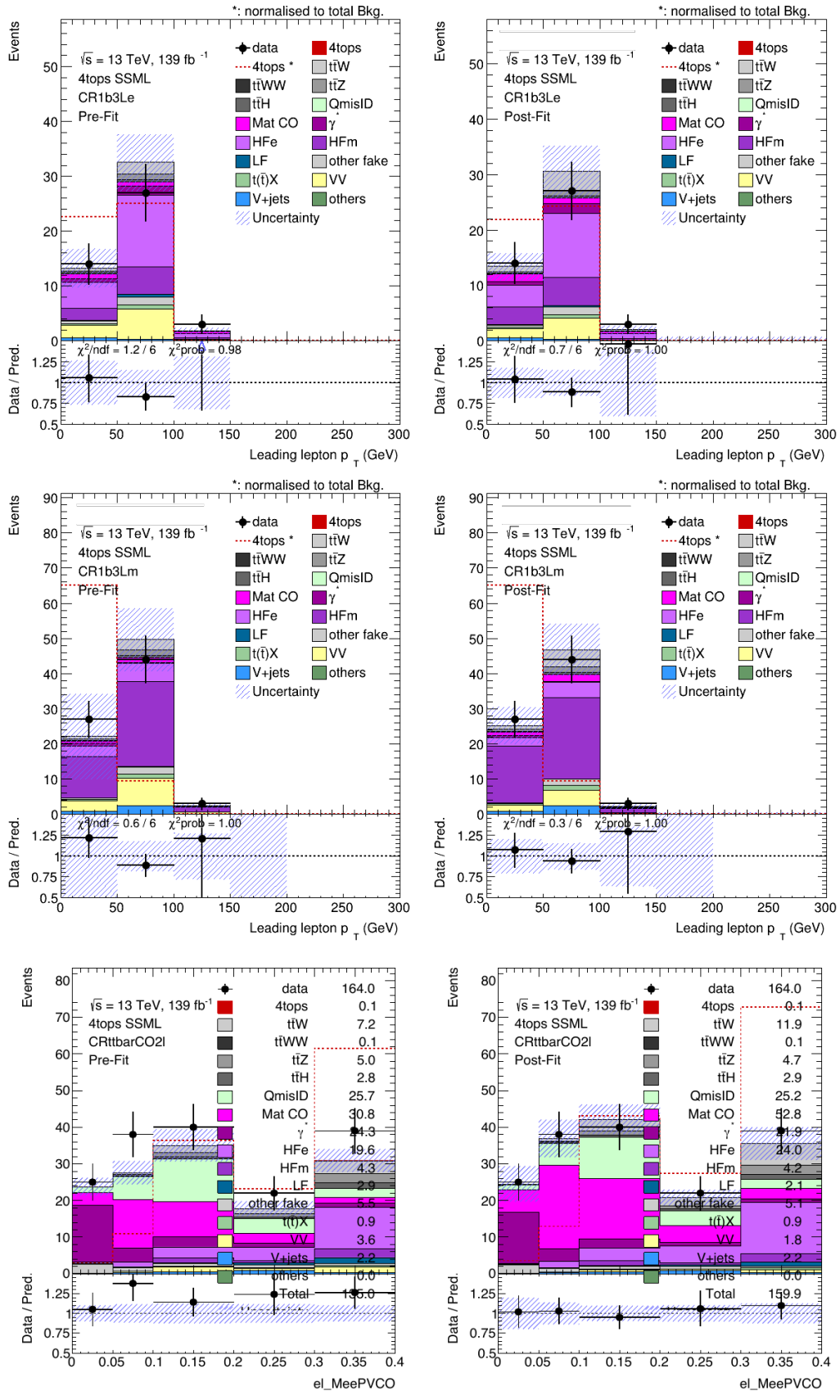

Figure 5.17: Control region plots comparing pre-fit (left) and post-fit (right) distributions for lepton p_T in 1b3le (top), lepton p_T in 1b3lm (middle), and invariant electron mass in CRttCO2l. Post-fit Data/MC shows good agreement.

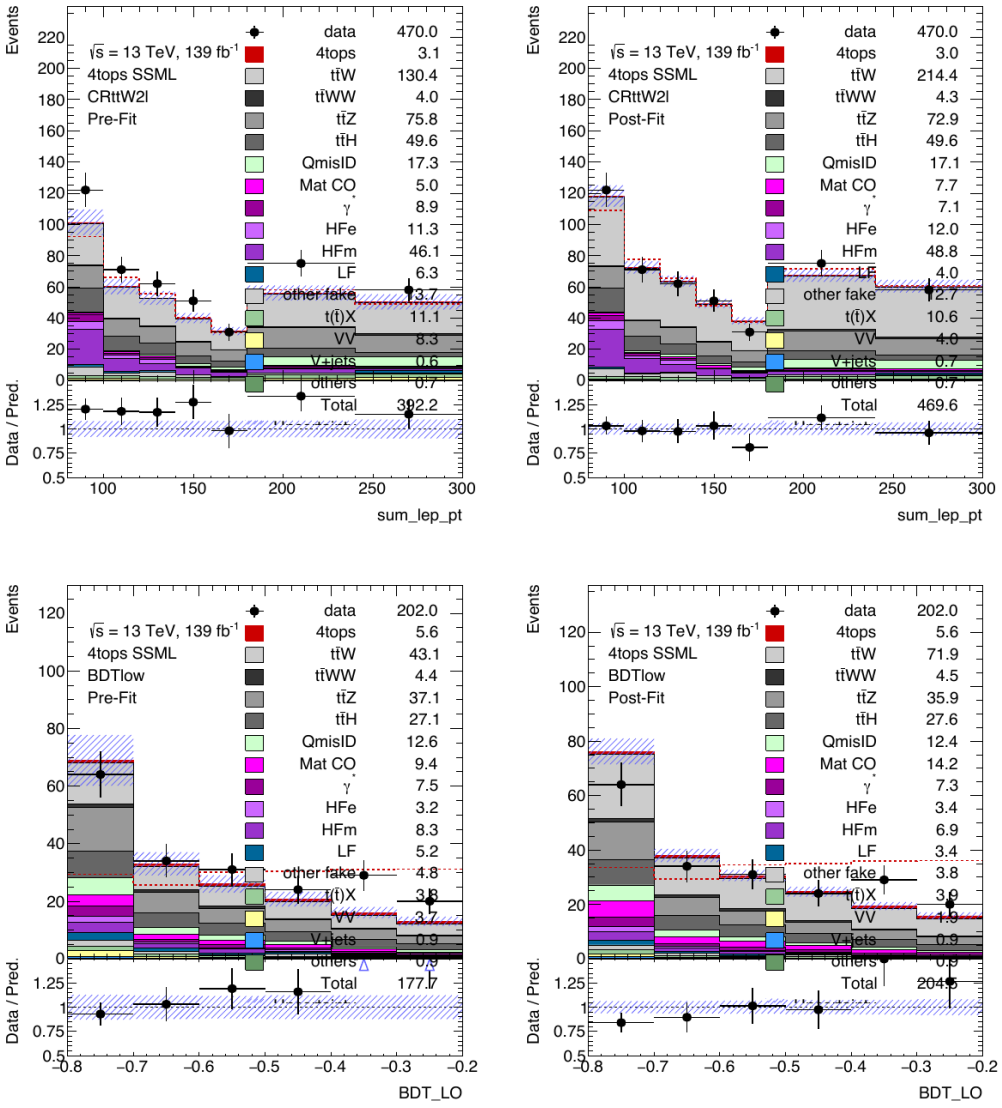

Figure 5.18: Control region plots comparing pre-fit (left) and post-fit (right) distributions for $\sum$ lepton p_T in CRttW2l (top) and the low end of the BDT distribution for CRBDTlow (bottom). Post-fit Data/MC shows good agreement.

5.5.2 Validation Region

A *Validation Region* (VR) is an area of phase space used to compare the data and Monte Carlo models in regions kinematically close to, but orthogonal to, the Signal Region. Once the Normalisation Factors have been obtained from the CRs, the fit is checked in the VR, to ascertain whether the normalisation is true for areas of phase space kinematically closer to the Signal Region. The VR in SSML counts the number of events in an area with the same jet and H_T constraints as the Signal Region, but instead uses the inverse of the Z-veto cut, where the two same-flavour leptons for three lepton events must have mass $81 < m_{\ell\ell} < 101$ GeV. Results of this fit are presented in Figure 5.19. It can be seen that the data and MC have good agreement, and therefore that the backgrounds have been well modelled for these regions, especially in the two leftmost bins of the $t\bar{t}W$ VR.

5.5.3 Monte Carlo Models

It is important that all signal and background events are modelled correctly. The production of $t\bar{t}t\bar{t}$ events is modelled using MadGraph5_aMC@NLO v2.6.2 [34], which provides matrix elements at next-to-leading order (NLO) in the strong coupling constant with the NNPDF3.1NLO [58] parton distribution function. Top quarks are decayed at leading order (LO) using MadSpin [59, 60]. The events are interfaced with Pythia8.230 [31] for the parton shower and hadronization, using the A14 set of tuned parameters [61] and the NNPDF23LO [58] PDF set. The decays of bottom and charm hadrons are simulated using EvtGen v1.6.0 [62].

To avoid using negative weights in the Boosted Decision Trees training, an additional $t\bar{t}t\bar{t}$ sample is produced at LO with the same MC settings used for the NLO sample. An additional $t\bar{t}t\bar{t}$ sample is also produced at NLO replacing the parton shower of the nominal samples to Herwig7.04 [32,33] to evaluate the impact of the parton shower and hadronization model.

The production of $t\bar{t}$ events is modelled using the PowhegBox [63–66] v2 generator at NLO with the NNPDF3.0NLO [58] PDF set and the h_{damp} parameter set to 1.5 m_{top} [67]. The events are interfaced with Pythia8.230 [31] using the A14 tune [61] and the NNPDF23LO PDF set.

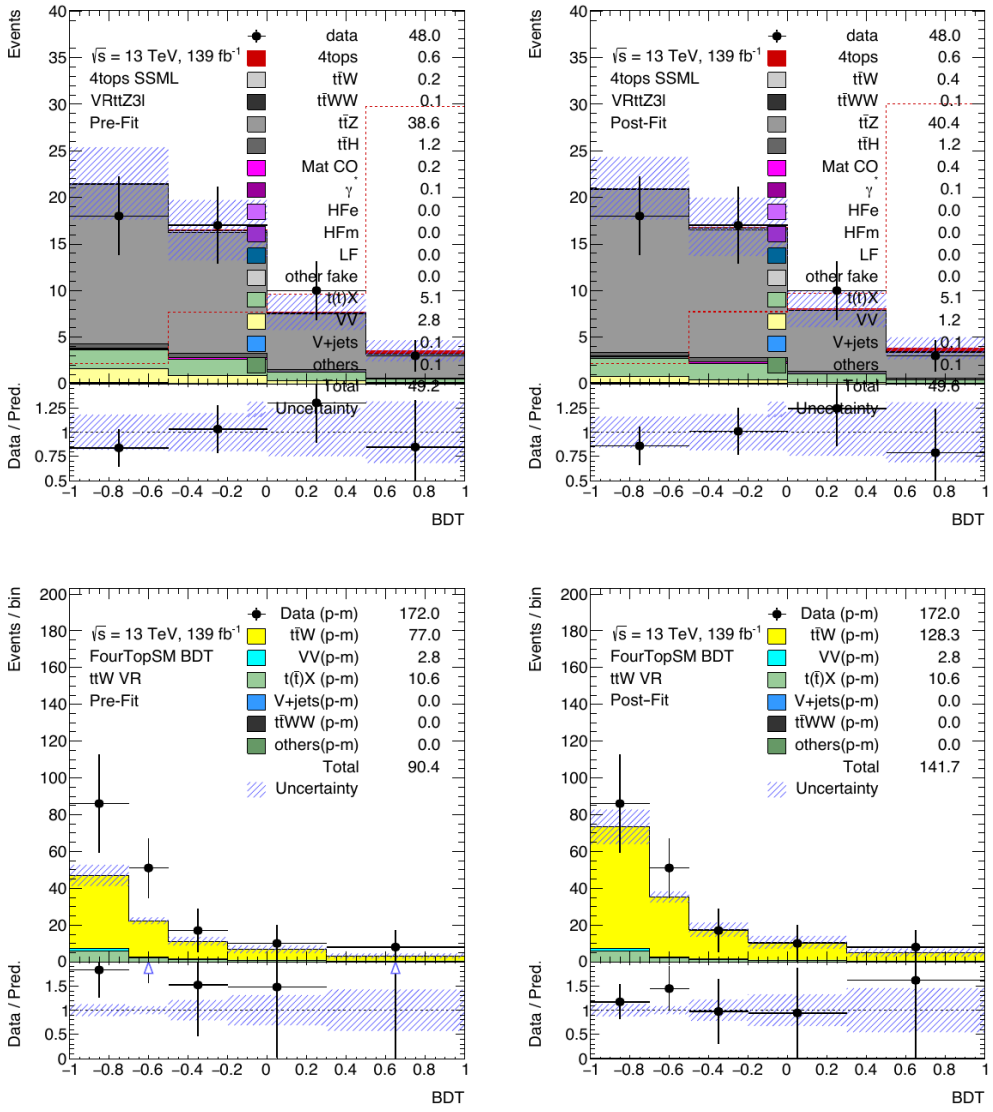

Figure 5.19: Validation region plots for pre-fit (left) and post-fit (right) distributions for $t\bar{t}Z$ (top) and $t\bar{t}W$ (bottom). Post-fit Data/MC shows good agreement.

5.6 Fit Results

Once the backgrounds were properly modelled, the data in the CR and VRs were fitted, again using TRExFitter. As the Signal Region is blinded, a number of different fits are performed in the Control Regions and propagated to the Signal Regions. Here, the signal strength, μ, is extracted, as well as the expected significance of this fit, σ. The fits are defined as;

- **Plain Asimov fit:** all signal and background regions are included and the pseudo-data used in the likelihood correspond exactly to the MC prediction. This allows fitted parameters (NFs) to be constrained, and an expected sensitivity based on pre-fit backgrounds to be extracted.

- **Real CRs-only fit:** only unblinded regions are included in this fit, and so real data is fitted. The goal of this fit is to derive a realistic post-fit background estimate without looking at data in the SR. By definition of the CRs, the signal should not contaminate this region and the normalisation is fixed to the SM prediction.

- **Realistic Asimov fit:** all signal and background regions are included in this fit and the pseudo-data correspond to the post-fit background prediction derived in the "real CRs-only fit" described above. No real data is directly used in this fit. The goal of this fit is to obtain the most probable values of the parameters pulls and constraints, as well as the expected sensitivity without looking at data.

- **Real SRs-blinded fit:** all regions are included in this fit. The only difference with respect to the "Realistic Asimov fit" is that observed data are used in the unblinded regions. In the blinded regions, pseudo-data corresponds to the post-fit background prediction derived in the "real CRs-only fit". This fit probes the effect of data fluctuations around the post-fit model on the parameters pulls and constraints, as well as on the expected sensitivity (for instance, $\mu_{\text{post-fit}} \neq 1$ as opposed to the "Realistic Asimov fit" for which $\mu_{\text{post-fit}} = 1$ by construction).

At the time of unblinding, the final region will be fitted with real data in all regions to obtain the final analysis signal strength and significance. The significance results with $\mu_{t\bar{t}t\bar{t}} = 1$ of the blinded analysis are presented here. $\mu_{t\bar{t}t\bar{t}} = 1$ assumes that the SM $t\bar{t}t\bar{t}$ signal has cross section $\sigma_{t\bar{t}t\bar{t}} = 11.97^{+18\%}_{-21\%}$ fb [41].

The results from the realistic Asimov fits are summarised in Table 5.12. These results show the expected data events in the Signal Region using a fit based on background data in the Control Regions. This gives an expected significance of 2.97σ. These parameters have all been independently floated in this fit.

Table 5.12: Expected signal ($t\bar{t}t\bar{t}$) and background (all other) yields in the SSML signal region, with all parameters floated individually.

Process	Yield in SR
$t\bar{t}t\bar{t}$	21.7 ± 8.7
$t\bar{t}W$	21.7 ± 6.3
$t\bar{t}WW$	2.2 ± 1.1
$t\bar{t}Z$	8.5 ± 1.9
$t\bar{t}H$	8.1 ± 2.1
QmisID	2.7 ± 0.2
Mat CO	3.5 ± 1.3
γ^*	0.9 ± 0.5
HFe	1.0 ± 0.8
HFm	2.0 ± 1.2
LF	0.6 ± 0.7
other fake	1.5 ± 0.7
t($\bar{t}$)X	1.0 ± 0.4
VV	0.2 ± 0.2
V+jets	0.03 ± 0.01
others	1.9 ± 1.7
Total	77.5 ± 7.7

5.6.1 Systematic Uncertainties

There are a large number of experimental and theoretical uncertainties that must be considered in the $t\bar{t}t\bar{t}$ analysis. A brief overview of those that have the largest contribution will be discussed here.

Experimental uncertainties arise from the LHC luminosity, and physics object reconstruction and identification. For the 2015-2018 run, the uncertainty on the integrated luminosity is 1.7% [68]. The reconstruction and identification uncertainties for electrons and muons differ for Monte Carlo and data, and these are accounted for using scale factors that are built into the generators, which are propagated throughout the analysis. Jet and E_T^{miss} uncertainties are modelled using nuisance parameters.

Modelling uncertainties are considered separately for the signal and backgrounds. For the $t\bar{t}t\bar{t}$ signal, uncertainties stem from missing higher-order QCD corrections, and parton showering in the Monte Carlo generator. The $t\bar{t}X$ backgrounds are considered similarly, however an uncertainty of 15% or 20% is applied to $t\bar{t}Z$ and $t\bar{t}H$ corss sections, respectively. For events with more than four b-jets, an uncertainty of 50% is applied to $t\bar{t}X$+jets backgrounds. Uncertainties for single top quark production is set to 30% for each process, while that of $t\bar{t}XX$ is set to 50%.

5.6.2 Signal Region

The overtraining check for the final BDT used in the fitting is shown in Figure 5.20 and it can be seen that in both odd and even testing, the BDT (points) is a good model for the sample (curve), especially at the high end where the signal is located. This BDT uses the 12 variables from Table 5.10 and parameters of nTrees = 800, Depth = 6, nmin = 3, Shrink = 0.01, Bagging = 0.7, to give a ROC integral of 0.854.

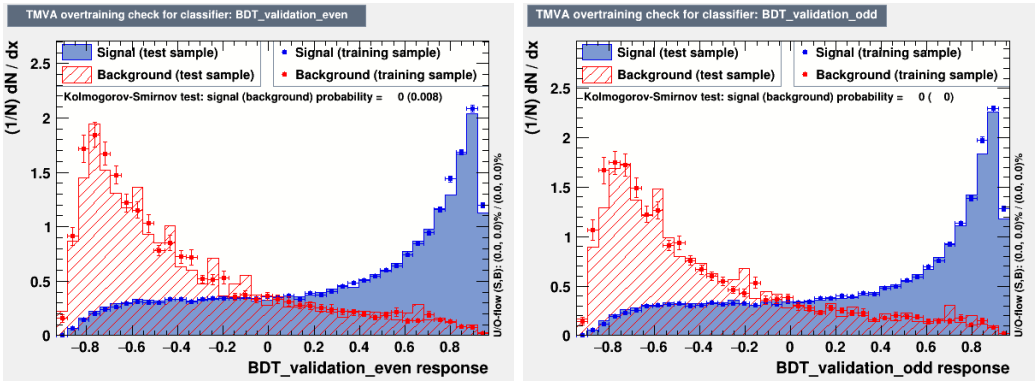

Figure 5.20: The final BDT validation plot to check for overtraining.

Pre- and post-fit plots for the 12 SR BDT variables are shown in Figures 5.21 through 5.24, which show good data/MC agreement in the Control and Validation Regions, and are a promising foundation for the Standard Model Four Top analysis, for which the unblinded results are highly anticipated. A summary of the current results for these fit regions can be found in Table 5.13, where "Split BDT" refers to separate fits for CRBDTLow and SR, which is due to the blinded data in the SR. The fits are performed with systematic and statistical errors.

Table 5.13: Expected $t\bar{t}t\bar{t}$ significances for the SSML channels.

	Plain Asimov	Realistic Asimov		Real SRs-blinded
	stat+syst	stat+syst	stat+syst (split BDT)	stat+syst (split BDT)
SSML	3.24	2.97	2.88	2.96

The results of the SSML channel will be combined with the 1LOS results – which are still currently blinded – to form a combined fit for the final unblinded analysis. The expected significance of 2.96σ suggests that this process may be present in the data. Once this is established, the value of $\mu_{t\bar{t}t\bar{t}}$ will influence how the cross section may be affected. Values above 1 would indicate that the cross section is higher than previously measured. This data could then be fitted again with the updated cross section to check the signal strength.

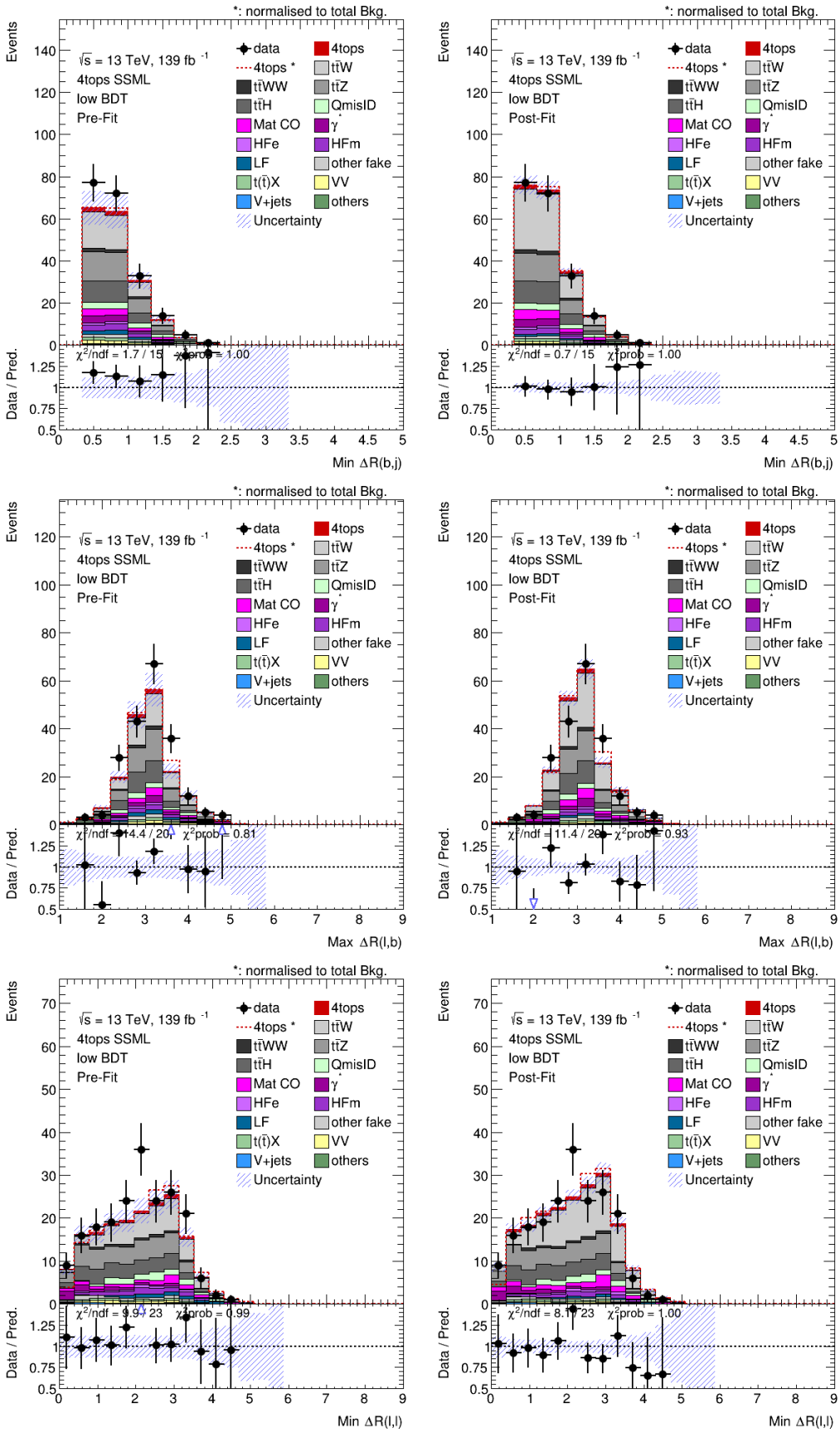

Figure 5.21: Signal region plots comparing pre-fit (left) and post-fit (right) distributions for BDT < -0.2 in MinΔR(b,j) (top), MaxΔR(l,b) (middle), and MinΔR(l,l) (bottom).

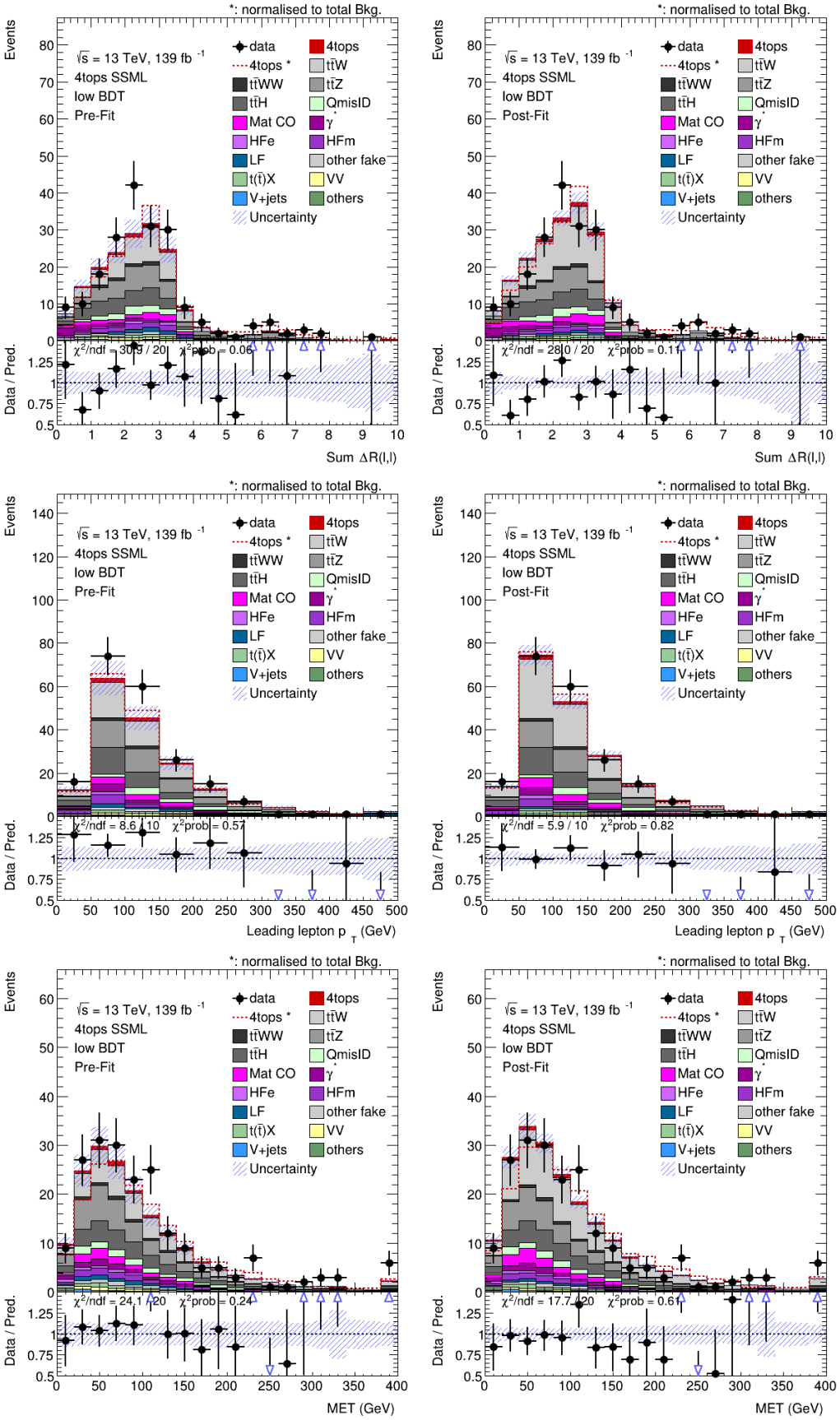

Figure 5.22: Signal region plots comparing pre-fit (left) and post-fit (right) distributions for BDT < -0.2 in $\sum \Delta R(\mathrm{l,l})$ (top), leading lepton p_T (middle), and missing transverse energy (bottom).

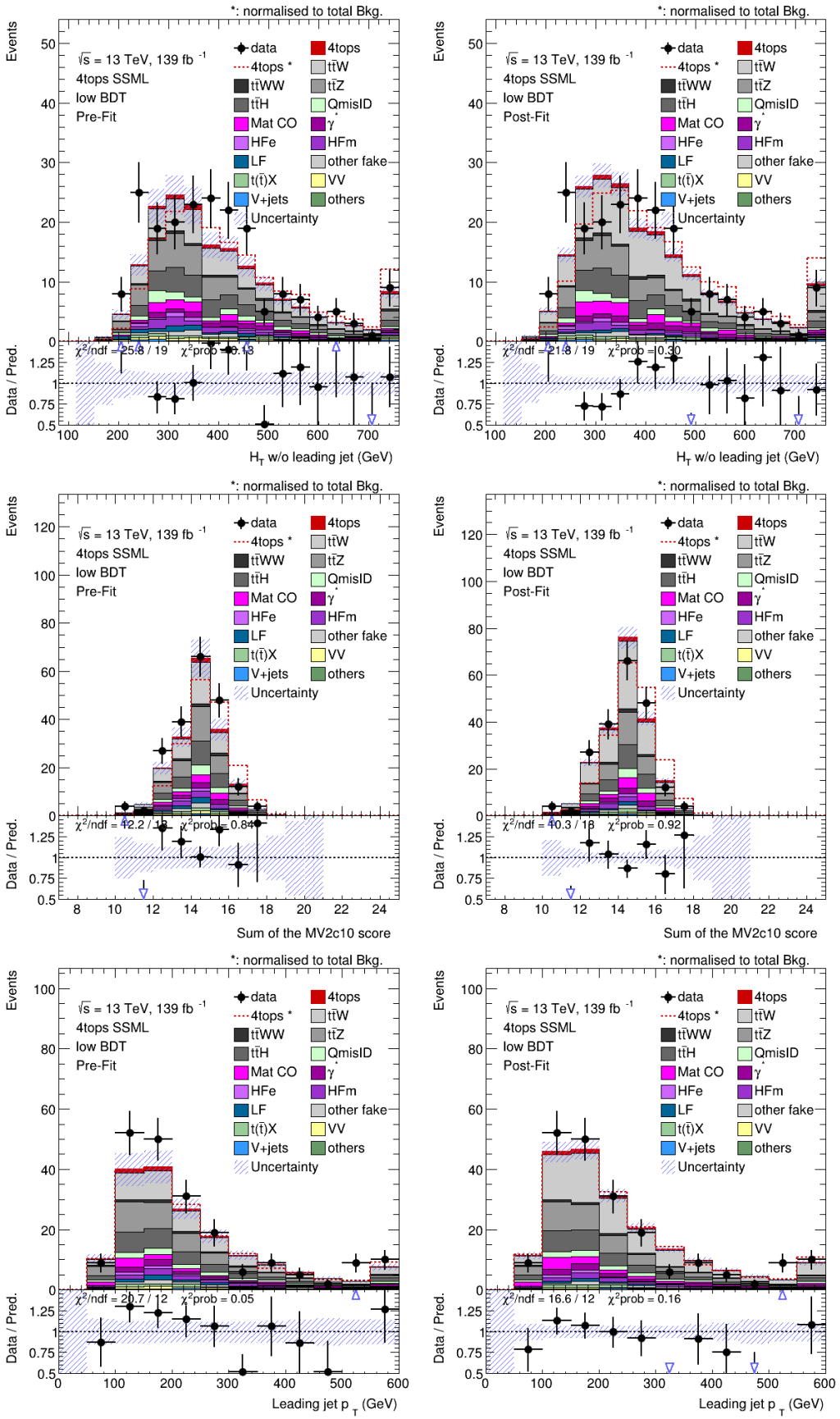

Figure 5.23: Signal region plots comparing pre-fit (left) and post-fit (right) distributions for BDT < -0.2 in $H_T$jets (no lead jet) (top), continuous b-tagging score (middle), and leading jet p_T (bottom).

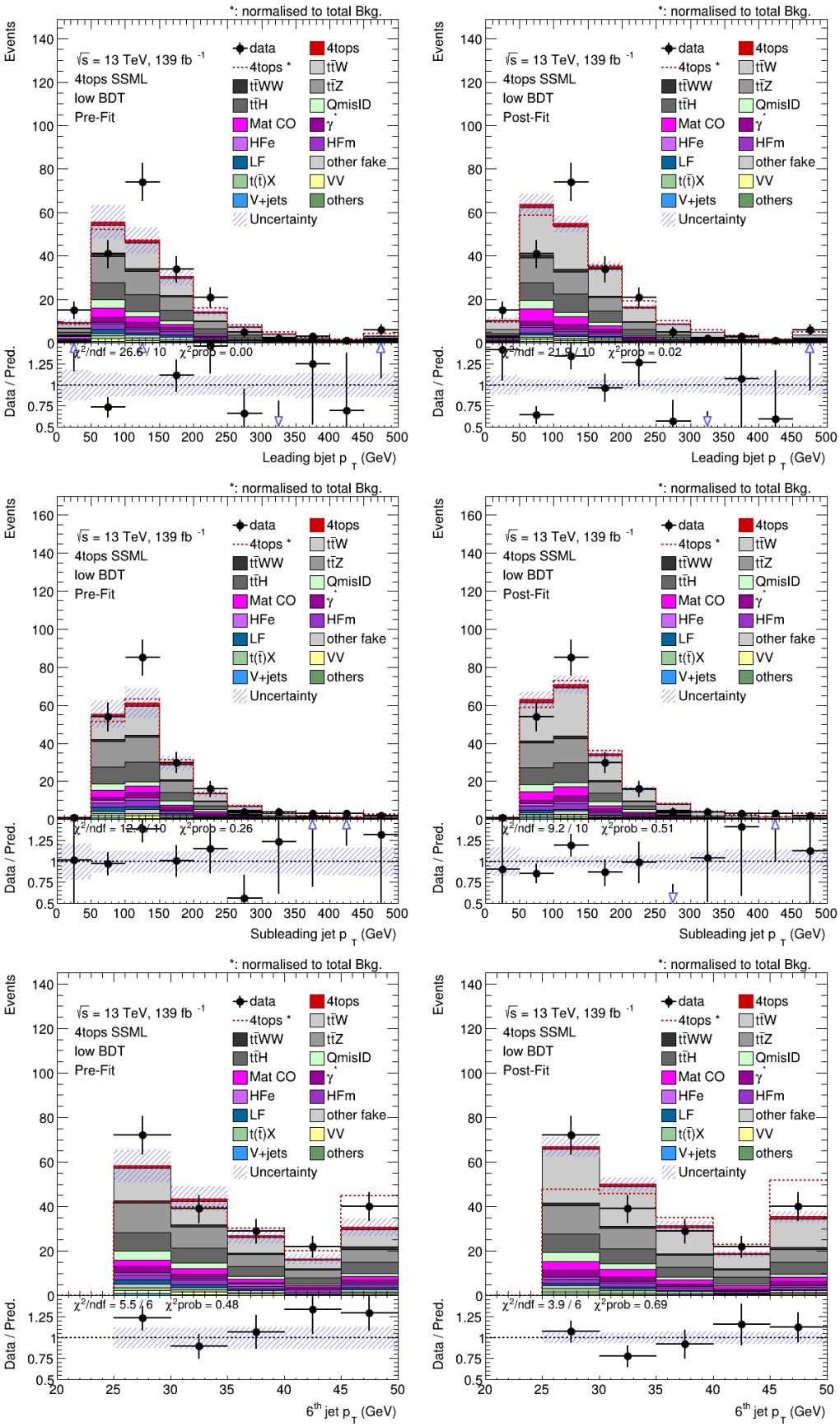

Figure 5.24: Signal region plots comparing pre-fit (left) and post-fit (right) distributions for BDT < -0.2 in leading b-jet p_T (top), 2nd lepton p_T (middle), and 6th lepton p_T (bottom).

Chapter 6

Conclusion

High energy particle physics at the Large Hadron Collider is entering a new era. Upgrades, especially to the Inner Tracker of the ATLAS detector will enable more data collection than ever before. This in turn will allow for more precise measurements of known Standard Model physics and the possibility of new analyses probing rare, or possibly beyond-standard-model, processes.

Establishing a test bench at the University of Adelaide opens many opportunities to be on the front line of these upgrades, especially in regards to testing and refining the data acquisition software and firmware for the Inner Tracker Pixel Modules. Documentation for this set-up is well under way and the Reconfigurable Cluster Element has been configured with the front-end RD53A emulator, and is interfaced with readout software. Once modules have been built, they will be able to be tested using this set-up. This space and its associated documentation will provide a repeatable experimental environment for the Pixel Modules to be tested before they are sent to the ATLAS detector.

In the Standard Model Four Top analysis, Boosted Decision Tree algorithms enabled a better understanding of the kinematic and variable distributions present in the same-sign multi lepton channel. Optimising this algorithm allowed for a better modelling of the background and signal Monte Carlo, which was seen in the overtraining plots, showing a comparable shape between tested and trained points in both signal and background regions. The algorithm was then applied to data, which has been fitted for the Control and Validation regions against Monte Carlo. Data in the Signal Region has not yet been fitted, but has been modelled using pseudo-data. The unblinded results of this analysis are highly anticipated, with an expected significance of 2.96σ. If this significance is realised, it will suggest evidence for the $t\bar{t}t\bar{t}$ process, which will allow further measurements of the four top process. The top quark's strong coupling to the Higgs boson gives potential for this process to be an excellent place to study beyond-standard-model physics, as it is the Higgs which is predicted to have the strongest coupling to new particles. The same-sign multi lepton channel is just one section of the current analysis, and it is expected that these results, combined with the one lepton opposite-sign channel, will further enhance the significance of the cross section measurement. Additional data collected in future LHC operations will greatly increase statistics available for further analysis of the four top standard model process.

Bibliography

[1] *Standard Model of Elementary Particles*, https://commons.wikimedia.org/wiki/File:Standard_Model_of_Elementary_Particles.svg. 2.1a

[2] E. Drexler, *Elementary particle interactions in the Standard Model*, https://commons.wikimedia.org/wiki/File:Elementary_particle_interactions_in_the_Standard_Model.png. 2.1b

[3] ATLAS Collaboration, *Measurement of the W-boson mass in pp collisions at $\sqrt{s} = 7$ TeV with the ATLAS detector.*, The European Physical Journal C **78** (2018), http://dx.doi.org/10.1140/epjc/s10052-017-5475-4. 2.1.2

[4] Particle Data Group Collaboration, M. Tanabashi et al, *Review of Particle Physics*, Phys. Rev. D **98** (2018) 030001, https://link.aps.org/doi/10.1103/PhysRevD.98.030001. 2.1.2, 2.1.2, 2.2.1, 5.1, 5.1, 5.2

[5] P. W. Higgs, *Broken Symmetries and the Masses of Gauge Bosons*, Phys. Rev. Lett. **13** (1964) 508–509, https://link.aps.org/doi/10.1103/PhysRevLett.13.508. 2.2.4

[6] F. Englert and R. Brout, *Broken Symmetry and the Mass of Gauge Vector Mesons*, Phys. Rev. Lett. **13** (1964) 321–323, https://link.aps.org/doi/10.1103/PhysRevLett.13.321. 2.2.4

[7] G. S. Guralnik, C. R. Hagen, and T. W. B. Kibble, *Global Conservation Laws and Massless Particles*, Phys. Rev. Lett. **13** (1964) 585–587, https://link.aps.org/doi/10.1103/PhysRevLett.13.585. 2.2.4

[8] ATLAS Collaboration, *Observation of a new particle in the search for the Standard Model Higgs boson with the ATLAS detector at the LHC.*, Physics Letters B **716** (2012). 2.2.4

[9] ATLAS Collaboration, *A particle consistent with the Higgs boson observed with the ATLAS detector at the Large Hadron Collider.*, Science (New York, N.Y.) (2012) 1576–82. 2.2.4

[10] CMS Collaboration, W. de Boer, *The Discovery of the Higgs Boson with the CMS Detector and its Implications for Supersymmetry and Cosmology*. 2013. arXiv:1309.0721 [hep-ph].

http://inspirehep.net/record/1252561/files/arXiv:1309.0721.pdf. 2.2

[11] CERN, *CERN: The accelerator complex*, https://public-archive.web.cern.ch/en/research/AccelComplex-en.html. 3.1

[12] CERN, *Linear accelerator 2 | CERN*, https://home.cern/science/accelerators/linear-accelerator-2. 3.1

[13] CERN, *The Proton Synchrotron | CERN*, https://home.cern/science/accelerators/proton-synchrotron. 3.1

[14] CERN, *The Super Proton Synchrotron | CERN*, https://home.cern/science/accelerators/super-proton-synchrotron. 3.1

[15] ATLAS Collaboration, *Luminosity determination in pp collisions at $\sqrt{s} = 13$ TeV using the ATLAS detector at the LHC*, Tech. Rep. ATLAS-CONF-2019-021, CERN, Geneva, Jun, 2019. http://cds.cern.ch/record/2677054. 3.1.1, 3.1.1

[16] ATLAS Collaboration, *Total Integrated Luminosity and Data Quality in 2015-2018*, https://twiki.cern.ch/twiki/bin/view/AtlasPublic/LuminosityPublicResultsRun2. 3.2

[17] ATLAS Collaboration, *Performance of the ATLAS track reconstruction algorithms in dense environments in LHC Run 2*, The European Physical Journal C **77** (2017), http://dx.doi.org/10.1140/epjc/s10052-017-5225-7. 3.1.2

[18] ATLAS Collaboration, *The ATLAS Experiment at the CERN Large Hadron Collider*, JINST **3** (2008) S08003. 3.3, 3.2, 3.6, 4.2

[19] ATLAS Collaboration, *Standard Model Summary Plots - July 2019*, https://atlas.web.cern.ch/Atlas/GROUPS/PHYSICS/PUBNOTES/ATL-PHYS-PUB-2019-024/. 3.4

[20] J. Pequenao, *Event Cross Section in a computer generated image of the ATLAS detector.*, Mar, 2008. 3.5

[21] ATLAS Collaboration, *Performance of missing transverse momentum reconstruction with the ATLAS detector using protonproton collisions at $\sqrt{s} = 13$ TeV*, The European Physical Journal C **78** (2018), http://dx.doi.org/10.1140/epjc/s10052-018-6288-9. 3.2

[22] ATLAS Collaboration, *Performance of electron and photon triggers in ATLAS during LHC Run 2*, Eur. Phys. J. **C80** (2020) 47, arXiv:1909.00761 [hep-ex]. 3.3.1

[23] ATLAS Collaboration, *Electron reconstruction and identification in the ATLAS experiment using the 2015 and 2016 LHC protonproton collision data at* $\sqrt{s} = 13$ *TeV*, The European Physical Journal C **79** (2019), http://dx.doi.org/10.1140/epjc/s10052-019-7140-6. 3.3.1

[24] ATLAS Collaboration, *Muon reconstruction performance of the ATLAS detector in protonproton collision data at* $\sqrt{s}$*ăTeV*, The European Physical Journal C **76** (2016), http://dx.doi.org/10.1140/epjc/s10052-016-4120-y. 3.3.1

[25] ATLAS Collaboration, *Measurement of the tau lepton reconstruction and identification performance in the ATLAS experiment using pp collisions at* $\sqrt{s} = 13$ TeV, Tech. Rep. ATLAS-CONF-2017-029, CERN, Geneva, May, 2017. https://cds.cern.ch/record/2261772. 3.3.1

[26] M. Cacciari, G. P. Salam, and G. Soyez, *The anti-ktjet clustering algorithm*, Journal of High Energy Physics **2008** (2008) 063063, http://dx.doi.org/10.1088/1126-6708/2008/04/063. 3.3.1, 3.3.2, 5.2.3

[27] F. Friedrich, *Tau Lepton Reconstruction and Identification at ATLAS*, EPJ Web of Conferences **28** (2012) 12007, http://dx.doi.org/10.1051/epjconf/20122812007. 3.3.1

[28] ATLAS Collaboration, *Jet energy scale measurements and their systematic uncertainties in proton-proton collisions at* $\sqrt{s} = 13\,TeV$ *with the ATLAS detector*, Physical Review D **96** (2017), http://dx.doi.org/10.1103/PhysRevD.96.072002. 3.3.2

[29] ATLAS Collaboration, *ATLAS b-jet identification performance and efficiency measurement with* $t\bar{t}$ *events in pp collisions at* $\sqrt{s} = 13\,TeV$, The European Physical Journal C **79** (2019), http://dx.doi.org/10.1140/epjc/s10052-019-7450-8. 3.3.2

[30] D. E. Soper, *Parton distribution functions*, Nuclear Physics B - Proceedings Supplements **53** (1997) 6980, http://dx.doi.org/10.1016/S0920-5632(96)00600-7. 3.4.1

[31] T. Sjöstrand, S. Ask, J. R. Christiansen, R. Corke, N. Desai, P. Ilten, S. Mrenna, S. Prestel, C. O. Rasmussen, and P. Z. Skands, *An Introduction to PYTHIA 8.2*, Comput. Phys. Commun. **191** (2015) 159–177, arXiv:1410.3012 [hep-ph]. 3.4.1, 5.5.3

[32] M. Bahr et al., *Herwig++ Physics and Manual*, Eur. Phys. J. C **58** (2008) 639–707, arXiv:0803.0883 [hep-ph]. 3.4.1, 5.5.3

[33] J. Bellm et al., *Herwig 7.0/Herwig++ 3.0 release note*, Eur. Phys. J. C **76** (2016) 196, arXiv:1512.01178 [hep-ph]. 3.4.1, 5.5.3

[34] J. Alwall, R. Frederix, S. Frixione, V. Hirschi, F. Maltoni, O. Mattelaer, H. S. Shao, T. Stelzer, P. Torrielli, and M. Zaro, *The automated computation of tree-level and next-to-leading order differential cross sections, and their matching to parton shower simulations*, JHEP **1407** (2014) 079, arXiv:1405.0301 [hep-ph]. 3.4.1, 5.5.3

[35] ATLAS Collaboration, *Technical Design Report for the ATLAS Inner Tracker Pixel Detector*, Tech. Rep. CERN-LHCC-2017-021. ATLAS-TDR-030, CERN, Geneva, Sep, 2017. https://cds.cern.ch/record/2285585. 4.1, 4.3

[36] E. Ward, *LHC and HL-LHC timeline for ATLAS website*, General Photo, Dec, 2018. 4.1

[37] ATLAS ITk Collaboration, M. Hamer, *Phase-II upgrade of the ATLAS Pixel Detector*, Tech. Rep. ATL-ITK-PROC-2019-005, CERN, Geneva, Mar, 2019. https://cds.cern.ch/record/2665116. 4.1.1

[38] D. Nelson, *HSIO II Development Platform Users Guide*, https://www.slac.stanford.edu/~djn/Atlas/HSIO_II/. 4.2, 4.5

[39] RD53 Collaboration, M. Garcia-Sciveres, *The RD53A Integrated Circuit*, Tech. Rep. CERN-RD53-PUB-17-001, CERN, Geneva, Oct, 2017. https://cds.cern.ch/record/2287593. 4.2

[40] T. Heim, *YARR: Yet Another Rapid Readout*, https://yarr.readthedocs.io/en/latest/. 4.2.3

[41] R. Frederix, D. Pagani, and M. Zaro, *Large NLO corrections in $t\bar{t}W^{\pm}$ and $t\bar{t}t\bar{t}$ hadroproduction from supposedly subleading EW contributions*, Journal of High Energy Physics **2018** (2018), arXiv:1711.02116. 5, 5.6

[42] Q.-H. Cao, S.-L. Chen, and Y. Liu, *Probing Higgs width and top quark Yukawa coupling from ttH and $t\bar{t}t\bar{t}$ productions*, Physical Review D **95** (2017), http://dx.doi.org/10.1103/PhysRevD.95.053004. 5.1

[43] ATLAS Collaboration, *Observation of the Top Quark*, Physical Review Letters **74** (1995) 26322637, http://dx.doi.org/10.1103/PhysRevLett.74.2632. 5.1

[44] ATLAS Collaboration, *Measurement of the $t\bar{t}$ production cross-section in the lepton+jets channel at $\sqrt{s} = 13$ TeV with the ATLAS experiment*, Tech. Rep. ATLAS-CONF-2019-044, CERN, Geneva, Sep, 2019. https://cds.cern.ch/record/2690717. 5.1

[45] S. Berlendis, F. Deliot, C. Nellist, E. Shabalina et al, *Search for $t\bar{t}t\bar{t}$ Standard Model Production in proton-proton collisions with the ATLAS Detector*, Tech. Rep. ATL-COM-PHYS-2019-302, CERN, Geneva, Apr, 2019. https://cds.cern.ch/record/2670354. 5.4, 5.5, 5.6, 5.7, 5.8

[46] ATLAS Collaboration, *Electron efficiency measurements with the ATLAS detector using the 2012 LHC proton–proton collision data*, ATLAS-CONF-2014-032, 2014, https://cds.cern.ch/record/1706245. 5.2.1

[47] ATLAS Internal, *Egamma Identification*, 2018. https://twiki.cern.ch/twiki/bin/view/AtlasProtected/EGammaIdentificationRun2. 5.2.1

[48] ATLAS Internal, *Lepton Isolation Working points*, 2018. https://twiki.cern.ch/twiki/bin/view/AtlasProtected/IsolationSelectionTool#Current_official_working_points. 5.2.1, 5.2.2

[49] ATLAS Internal, *Electron Charge ID Selection*, 2018. https://twiki.cern.ch/twiki/bin/view/AtlasProtected/ElectronChargeFlipTaggerTool. 5.2.1

[50] ATLAS Internal, *MCP Analysis Guidelines*, 2018. https://twiki.cern.ch/twiki/bin/view/AtlasProtected/MCPAnalysisWinterMC16. 5.2.2

[51] W. Lampl et al., *Calorimeter Clustering Algorithms: Description and Performance*, ATL-LARG-PUB-2008-002, 2008, https://cds.cern.ch/record/1099735. 5.2.3

[52] ATLAS Collaboration, *Tagging and suppression of pileup jets with the ATLAS detector*, ATLAS-CONF-2014-018, 2014, https://cds.cern.ch/record/1700870. 5.2.3

[53] ATLAS Internal, *Jet Vertex Tagger Tool*, 2018, https://twiki.cern.ch/twiki/bin/view/AtlasProtected/JetVertexTaggerTool. 5.2.3

[54] ATLAS Collaboration, *Expected performance of the ATLAS b-tagging algorithms in Run-2*, ATL-PHYS-PUB-2015-022, 2015, https://cds.cern.ch/record/2037697. 5.2.3

[55] ATLAS Collaboration, *Recommendations of the Physics Objects and Analysis Harmonisation Study Groups 2014*, Tech. Rep. ATL-PHYS-INT-2014-018, CERN, Geneva, Jul, 2014. https://cds.cern.ch/record/1743654. 5.2.5

[56] A. Hoecker, P. Speckmayer, J. Stelzer et al., *Toolkit for Multivariate Data Analysis with ROOT*, tech. rep., 2005. https://root.cern.ch/download/doc/tmva/TMVAUsersGuide.pdf. 5.4.1, 5.4.1

[57] *TRExStats/TRExFitter*, https://gitlab.cern.ch/TRExStats/TRExFitter. 5.5.1

[58] NNPDF Collaboration, NNPDF Collaboration, R.D. Ball et al., *Parton distributions for the LHC Run II*, JHEP **04** (2015) 040, arXiv:1410.8849 [hep-ph]. 5.5.3

[59] S. Frixione, E. Laenen, P. Motylinski, and B. R. Webber, *Angular correlations of lepton pairs from vector boson and top quark decays in Monte Carlo simulations*, JHEP **0704** (2007) 081, arXiv:hep-ph/0702198. 5.5.3

[60] P. Artoisenet, R. Frederix, O. Mattelaer, and R. Rietkerk, *Automatic spin-entangled decays of heavy resonances in Monte Carlo simulations*, JHEP **1303** (2013) 015, arXiv:1212.3460 [hep-ph]. 5.5.3

[61] ATLAS Collaboration, *ATLAS Pythia 8 tunes to* 7 *TeV data*, ATL-PHYS-PUB-2014-021, 2014, https://cds.cern.ch/record/1966419. 5.5.3

[62] D. J. Lange, *The EvtGen particle decay simulation package*, Nucl. Instrum. Meth. A **462** (2001) 152. 5.5.3

[63] S. Frixione, P. Nason, and G. Ridolfi, *A Positive-weight next-to-leading-order Monte Carlo for heavy flavour hadroproduction*, JHEP **09** (2007) 126, arXiv:0707.3088 [hep-ph]. 5.5.3

[64] P. Nason, *A New method for combining NLO QCD with shower Monte Carlo algorithms*, JHEP **0411** (2004) 040, arXiv:hep-ph/0409146. 5.5.3

[65] S. Frixione, P. Nason, and C. Oleari, *Matching NLO QCD computations with Parton Shower simulations: the POWHEG method*, JHEP **11** (2007) 070, arXiv:0709.2092 [hep-ph]. 5.5.3

[66] S. Alioli, P. Nason, C. Oleari, and E. Re, *A general framework for implementing NLO calculations in shower Monte Carlo programs: the POWHEG BOX*, JHEP **1006** (2010) 043, arXiv:1002.2581 [hep-ph]. 5.5.3

[67] ATLAS Collaboration, *Studies on top-quark Monte Carlo modelling for Top2016*, ATL-PHYS-PUB-2016-020, 2016, https://cds.cern.ch/record/2216168. 5.5.3

[68] G. Avoni et al., *The new LUCID-2 detector for luminosity measurement and monitoring in ATLAS*, JINST **13** (2018) P07017. 5.6.1